2011

VIABILITY OF A CONTROLLABLE CHAOTIC MICROMIXER THROUGH THE USE OF TITANIUM-NICKEL SHAPE MEMORY ALLOY

David Ryan Lilly
University of Kentucky, lilly.ryan1@gmail.com

STUDENT AGREEMENT:

I represent that my thesis or dissertation and abstract are my original work. Proper attribution has been given to all outside sources. I understand that I am solely responsible for obtaining any needed copyright permissions. I have obtained and attached hereto needed written permission statements(s) from the owner(s) of each third-party copyrighted matter to be included in my work, allowing electronic distribution (if such use is not permitted by the fair use doctrine).

I hereby grant to The University of Kentucky and its agents the non-exclusive license to archive and make accessible my work in whole or in part in all forms of media, now or hereafter known. I agree that the document mentioned above may be made available immediately for worldwide access unless a preapproved embargo applies.

I retain all other ownership rights to the copyright of my work. I also retain the right to use in future works (such as articles or books) all or part of my work. I understand that I am free to register the copyright to my work.

REVIEW, APPROVAL AND ACCEPTANCE

The document mentioned above has been reviewed and accepted by the student's advisor, on behalf of the advisory committee, and by the Director of Graduate Studies (DGS), on behalf of the program; we verify that this is the final, approved version of the student's dissertation including all changes required by the advisory committee. The undersigned agree to abide by the statements above.

David Ryan Lilly, Student

Dr. Christine Trinkle, Major Professor

Dr. James McDonough, Director of Graduate Studies

VIABILITY OF A CONTROLLABLE CHAOTIC MICROMIXER THROUGH THE USE OF TITANIUM-NICKEL SHAPE MEMORY ALLOY

THESIS

A thesis submitted in partial fulfillment of the
Requirements for the degree of Master of Science in
Mechanical Engineering in the College of
Engineering at the University of Kentucky

By

David Ryan Lilly

Lexington, Kentucky

Director: Dr. Christine Trinkle, Professor of Mechanical Engineering

Lexington, Kentucky

2011

ABSTRACT OF THESIS

VIABILITY OF A CONTROLLABLE CHAOTIC MICROMIXER THROUGH THE USE OF TITANIUM-NICKEL SHAPE MEMORY ALLOY

Microfluidic devices have found applications in a number of areas, such as medical analysis, chemical synthesis, biological study, and drug delivery. Because of the small channel dimensions used in these systems, most microchannels exhibit laminar flow due to their low Reynold's number, making mixing of fluids very challenging. Mixing at this size scale is diffusion-limited, so inducing chaotic flow patterns can increase the interface surface area between two fluids, thereby decreasing overall mixing time.

One method to create a chaotic flow within the channel is through the introduction of internal protrusions into the channel. In such an application protrusions that create a rotational flow within the channel are preferred due to their effectiveness in folding the two fluids over one another. The novel mixer outlined in this paper uses a Ti-Ni shape memory alloy for the creation of protrusions that can be turned controlled through material temperature. Controllability of the alloy allows users to turn the chaotic flow created by the protrusions off and on by varying the temperature of the mixer. This ability contributes to the idea of a continuous microfluidic system that can be turned on only when necessary as well as recycle unmixed fluids while turned off.

KEYWORDS: Chaotic Micomixer, Microfluidic, Shape Memory Alloy, Micro-Fabrication.

David Ryan Lilly

12/16/2011

(Date)

VIABILITY OF A CONTROLLABLE CHAOTIC MICROMIXER THROUGH THE USE OF TITANIUM-NICKEL SHAPE MEMORY ALLOY

By

David Ryan Lilly

Dr. Christine Trinkle
Director of Thesis

Dr. James McDonough
Director of Graduate Studies

Date

TABLE OF CONTENTS

LIST OF TABLES

LIST OF FIGURES

Chapter 1: Introduction

1.1 Microfluidics

Microfluidics concerns the manipulation of fluids with sub-millimeter dimensional constraints. Microfluidic systems are becoming increasingly popular in applications involving miniature analytical devices, biomedical devices as well as many other areas of biotechnology. These systems are becoming more popular in commercial applications and research in academia. Due to the many advantages of microfluidic systems. Sub-millimeter size constraints allow for smaller volumes of samples and reagents to be used, shorter analysis times, higher throughput and lower manufacturing costs [1]. These properties lend themselves to lab-on-a-chip systems that are capable of environmental monitoring, cell separation, DNA-sequencing and many other analytical applications [2]. Although the advantages and applications are almost limitless for microfluidic systems, there are several obstacles that arise when you are manipulating fluids on the sub-millimeter scale that must be overcome in order to realize its full potential.

One of the complications faced when using a microfluidic system concerns the ability to mix two or more fluids on the sub-millimeter scale. Micro-scale fluid flows are inherently laminar, so the only mixing that is present between two fluids in a channel occurs through diffusion at the boundary between the fluids. This is not a limitation when working on a larger scale where vortices and turbulence are naturally created within a given channel allowing the fluids to chaotically mix by folding the fluids over one another. Furthermore, external devices such as rotating mixing blades or high

pressure jets that can actively aid in the mixing of the fluids are difficult to fabricate and utilize in the micro-scale domain. Since mixing is a vital part of many proposed micro analytical systems, the question of how to mix efficiently within the dimensional constraints of such a system has become a key area of research.

1.2 Micro-Scale Fluid Behavior

As discussed previously, the fluid mechanics of a microfluidic system has a completely laminar from as compared to a turbulent flow seen in a typical macro scale fluid flow. This is due to the low Re number and negligible inertial forces. Reynolds numbers in microfluidic channels are often observed to be Re=4 or less due to the length and velocity of the system decreasing significantly in comparison with larger channels. Since transition from laminar to turbulent flow is around a Re=2000 [3] turbulent flow is not often seen in microfluidics without the presence of larger driving forces. This allows for the inertial forces to be ignored giving a simplified version of the Navier-Stokes equation (1-1) called the Stokes/Creeping Flow equation (1-2) shown below [3]. Variables for equations (1-1), (1-2) and (1-3) are as follows: ρ=density, u=velocity field, p=pressure, μ=dynamic viscosity, f=force and v=mean velocity.

$$\rho \frac{d\mathbf{u}}{dt} = -\nabla p + \rho \mathbf{f} + \mu \nabla^2 \mathbf{u} \tag{1-1}$$

$$\nabla p = \rho \mathbf{f} + \mu \nabla^2 \mathbf{u} \tag{1-2}$$

$$Re = \frac{\rho \mathrm{vL}}{\mu} \tag{1-3}$$

The resulting flow present in a system that exhibits Stokes flow is completely laminar and can be advantageous in many instances but is a major hindrance in the development of an efficient micromixer.

1.3 Micromixers

A micromixer is a device designed to mix two or more fluids within the dimensional constraints of the micro-scale. The largest obstacle faced when designing a micromixer is that the fluids experience only laminar flow. This limits any mixing between two fluids to diffusion through the singular plane in which the fluids meet. The length of channel required to fully mix two liquids based solely on diffusion is governed by the width of the channel, diffusion coefficients of the liquids and the velocity of the liquids. This length is often characterized by the dimensionless ratio called the Peclet number [4], defined in equation (1-4). The Peclet number (*Pe*) is a function of the fluid velocity (*U)*, channel width (*l), and* molecular diffusivity (*D*).

$$Pe = \frac{Ul}{D} \tag{1-4}$$

Using these variables, it is possible to approximate the required length (*L*) (1-5) to achieve complete mixing by estimating the time necessary for diffusion across the channel multiplied by the flow velocity [5]:

$$L \approx U \times \frac{l^2}{D} \tag{1-5}$$

From these equations the Peclet number and approximate mixing length can be calculated given a typical diffusion $D=10^{-10}$ m^2/s (water) as well as typical velocity and width of

1cm/s and 100μm. This gives a Pe=10^4 and an approximate mixing length of 1 meter which is much larger than the width and height of the channel. A long mixing path is difficult to incorporate into a compact surface, which negates one of the advantages gained by using a microfluidic system. For this reason, many different designs for micromixers have developed in the past decade.

Micromixers can be subdivided into two categories, active and passive. Active mixers operate by using an external driving force to create disturbances in the flow to mix the fluid within the channel. Passive mixers operate only on diffusion and chaotic advection and do not require external energy [1]. Both types of mixers have advantages and disadvantages associated with the methods used to induce mixing within the channel.

1.3.1 Active Micromixers

Active micromixers are devices that use an external force to create a disturbance that initiates mixing between two or more fluids on the micrometer scale. There are many methods that have been used to actively effect mixing in mircochannels. Active micromixers in recent years have been found to be very efficient over relatively short distances through the use of external disturbances such as pressure waves, temperature changes, magnetohydrodynamic forces, acoustic waves and electrohydrodynamic forces [1].

Despite their efficiency, there are several drawbacks to an active system. Because these systems require an outside disturbance, integrated components are needed to create the disturbance. Active components also require an external power source to be connected to the system. This can lead to complex systems that are difficult to

manufacture, often large and can have a high manufacturing cost. The potentially large size can greatly hinder the integration of the component into a larger system.

1.3.1.1 Pressure Disturbance

Pressure disturbance micromixer designs were some of the earliest active mixers due to their relatively simple design compared with other active mixing methods [1]. Mixing is caused by disrupting the pressure of the entering fluids, which in turn disrupts the flow leading to an increase in mixing efficiency. This type of micromixer most often is designed using a low Reynolds number flow allowing for a predictable flow pattern between the two fluids.

One such design uses pulsing micropumps to increase the diffusion interface between the two fluids [11]. By controlling the relative fluid velocity of two fluids with separate pumps as they enter a mixing chamber, a pressure difference between the two streams can be created giving way to a non-linear diffusion interface. Alternatively, a disturbance can be introduced through a pulsing velocity introduced from a side inlet on the mixing chamber. Instead of completely stopping one of the pumps, the velocity is varied in one fluid creating the same type of non-linear segmented flow illustrated in Figure 1.1 [12].

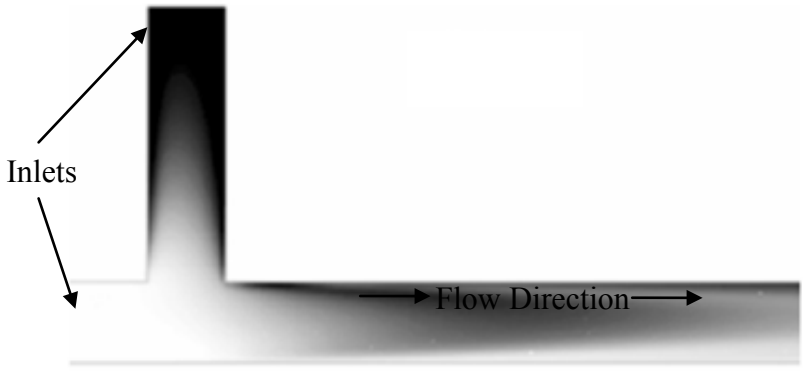

Figure 1.1: Pressure disturbance: Velocity pulsing side flow. The segmented flow created by a pressure disturbance system can be seen in the above image. By segmenting the fluid, a large surface area interface for diffusion is created greatly increasing mixing efficiency. Image adapted from [12].

1.3.1.2 Acoustic Disturbance

Another example of an active mixing technique is an acoustic disturbance system. Unlike pressure disturbance systems, this method does not require careful control of flow velocity or pressure. Active mixing is caused by acoustic waves being externally introduced to the mixing channel or chamber to induce a mixing motion. In figure 1.2 acoustic waves were introduced to a mixing chamber from below inducing mixing within the chamber. This has been done by using ultra-sonic waves to effect mixing but has limited application due to the increased temperature caused by the system [13].

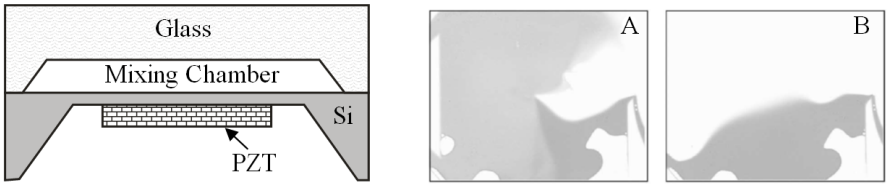

Figure 1.2: Schematic of ultrasonic mixing system: using piezoelectric vibration source. (A) Mixing chamber after PZT on for 7 seconds. (B) Mixing chamber with PZT turned off. Figure adapted from [13].

Other methods investigated have consisted of acoustic streaming to excite a bubble within the mixing chamber or channel [14], as shown in Figure 1.3. A piezoelectric disk excites an air bubble trapped in the microfluidic device, creating convection flow within the mixing chamber. Although there is a clear convective flow present, the time needed to show complete mixing was large

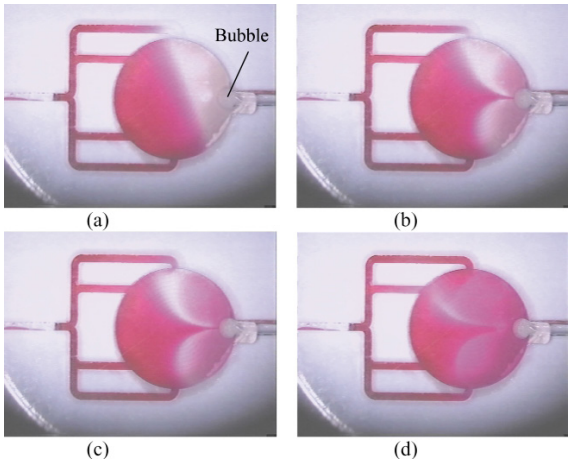

Figure 1.3: Bubble excitation micromixer: (a) 0s, (b) 15s, (c) 35s, (d) 70s. Figure adapted from [14].

1.3.1.3 Other Active Micromixers

Many other active micromixers in addition to the designs already discussed work on the basic principle of generating an external disturbance to disrupt a microflow to induce mixing. Methods using electrodes within the channel using varying voltage to create efficient mixing have been investigated [15]. Other novel designs use a magnetic field to induce mixing with electrolyte solutions [16]. Investigation into thermal disturbance has also been a topic of research due to the diffusion coefficient of most liquids is dependent on temperature in turn affecting overall mixing efficiency [17].

These examples represent only a few of the many designs that utilize various external disturbances to achieve active mixing. In general, although many active designs have reported efficient mixing, the designs are often complex, making them difficult and expensive to incorporate into microfluidic devices.

1.3.2 Passive Micromixers

Passive micromixers can be characterized as devices that use only diffusion and chaotic advection to initiate mixing between two or more fluids in a laminar microscale flow. Passive devices work by increasing the contact surface area between two fluids; since diffusion is the only means of mixing in a laminar microchannel, increasing the contact surface are increases the amount of diffusion increasing mixing efficiency several methods have been explored to create the increase in contact surface area or chaotic advection needed for quick and efficient mixing. The various methods can be broken down into four sub-categories of passive mixers: parallel lamination, serial lamination, injection, and chaotic advection systems [1].

1.3.2.1 Parallel and Serial Lamination

Lamination mixing is accomplished by splitting the two inlet fluids to be mixed into N streams and recombining the split flows to create the desired increased contact surface area for mixing. Both parallel and serial lamination systems use this same principle in slightly different ways. Parallel lamination splits the entrance flows into N streams in a single direction and combines the flow with alternating streams of each of the two fluids [1], as shown in Figure 1.4b. Designs of such parallel lamination mixers

vary widely and are only hindered by the increasingly complex geometry, which correlates to increasing N; mixers with as high as 32 laminations have been reported [8]. Figure 1.4 (b) illustrates this type of parallel lamination mixer.

Another method to effect parallel lamination is to narrow the width of the channel so the distance required for complete diffusion is greatly minimized [7], as shown in Figure 1.4a. The reduced distance required for mixing is reflected in a lower Peclet. Since the calculation for the Peclet number uses the width in the numerator and decreased width will lead to a smaller Peclet number. This is because the Peclet number relates the time taken for the fluid to diffuse across the channel to the velocity of the flow. Since diffusion rate is independent of width a smaller width will yield shorter mixing distances. Figure 1.4 (a) shows this type of lamination design.

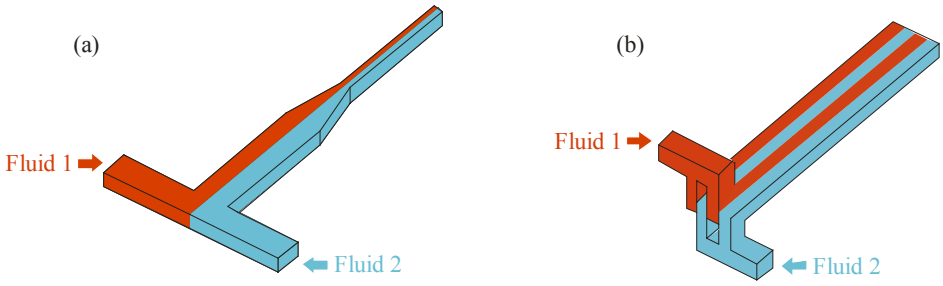

Figure 1.4: Parallel lamination mixers: (a) narrow lamination (b) multiple stream lamination.

Serial lamination uses the same principle as parallel lamination, but first joins the two fluids then splits the stream and later rejoins to increase in contact surface area, as shown in Figure 1.5. Often the streams are joined horizontally and then vertically in an alternating pattern; by doing this the contact surface area is greatly increased by creating multiple streams of each fluid.

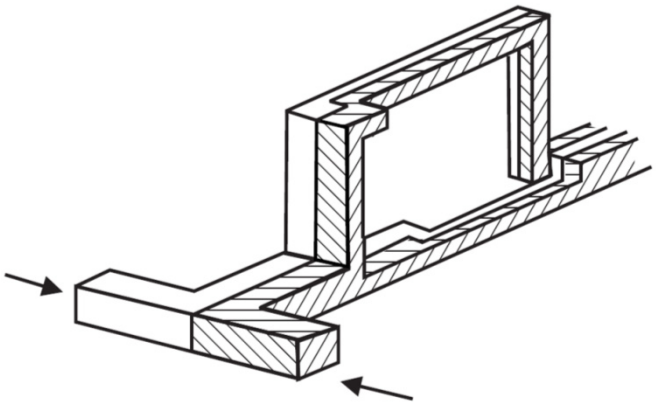

Figure 1.5: Serial lamination mixers: Flow splits and re-combines in varying directions.

1.3.2.2 Injection

Injection mixing uses similar principles to that of lamination but splits the solute into multiple streams to be injected into a larger solvent stream. The efficiency of this type of mixer is only limited by the combination of the number of inlets that can be fabricated and the diffusion of the solute and solvent. Many designs for this type of mixer have been studied including designs with large arrays of nozzles [9]. This method greatly increases the available surface area for diffusion between the two media. Figure 1.6 illustrates a possible design for an injection micromixer.

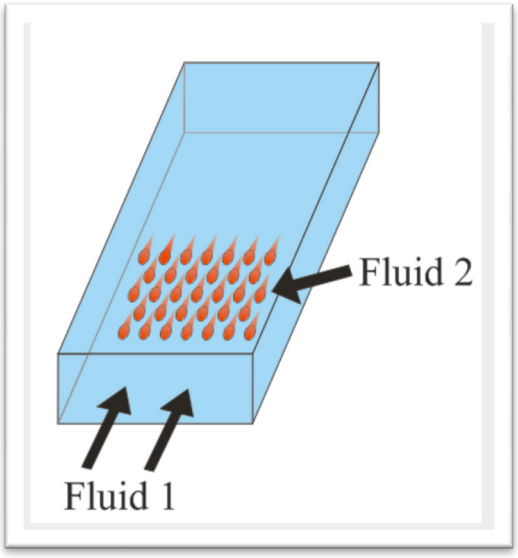

Figure 1.6: Injection mixers: nozzle injection.

1.3.2.3 Chaotic Advection

Advection is the transport of a substance by the bulk movement of a fluid; in most microfluidic channels advection occurs parallel to the direction of the primary direction of flow due to the lack of turbulent flow. Chaotic advection is produced by forming a chaotic fluid flow within the channel. The chaotic flow of the fluid transports the substance in directions other than that of the dominant flow direction creating an increased mixing effect. By creating chaotic advection within the channel the mixing distances required can be greatly reduced.

Although chaotic advection is used widely in active mixers, it is also used in passive mixers by altering the internal geometry of the channel or adding geometrical features to affect a chaotic flow within the channel. It is the resulting chaotic flow that folds and splits the flow creating a greater contact surface area for diffusion resulting in an efficient micromixer. This type of mixer can be achieved using many different

designs; Figure 1.7 and 1.8 illustrate several designs that have been previously studied for microfluidic flows with high and low Reynolds numbers respectively.

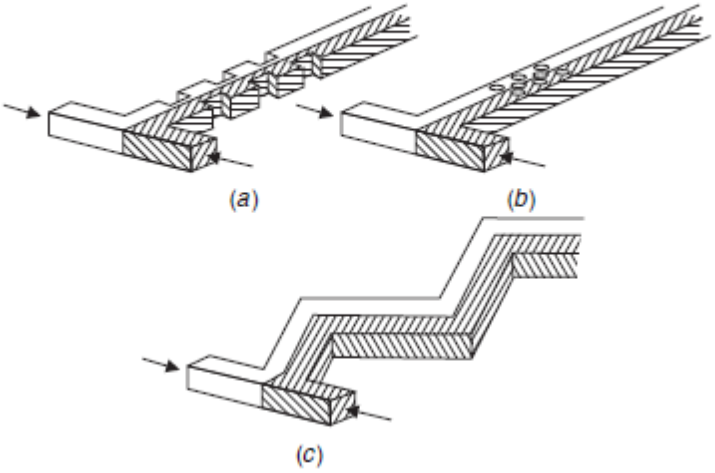

Figure 1.7: High Reynolds number designs: (a) obstacles on the wall; (b) obstacles in the channel; (c) zig-zig or serpentine channels. Figure adapted from [1].

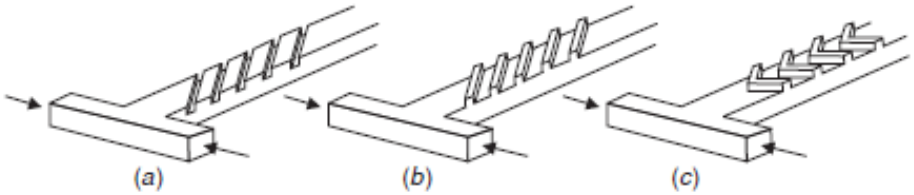

Figure 1.8: Low Reynolds number designs: (a) Slanted Ribs; (b) Slanted Grooves; (c) Herringbone Grooves. Figure adapted from [1].

The basic goal of a chaotic micromixer is to create a chaotic fluid flow, but the geometry needed to accomplish this is depends on whether the flow has a high or low Reynolds number. Although higher fluid velocities can create a higher Reynolds number flow in a microchannel, they still often display laminar flow in featureless channels. To create a chaotic flow, it is necessary to introduce elements such as barriers or direction changes in the channel as illustrated in Figure 1.7. Such elements will aid in creating a chaotic flow in the presence of a high velocity/Reynolds since any resistance (barrier, direction change) in the flow will create turbulence. Such internal features are more

effective in the presence of high velocity/Reynolds number flows since inertial forces have a much larger influence than in a low Reynolds number flow.

Conversely, at lower Reynolds numbers geometric elements such as those shown in Figure 1.7 will not always significantly affect the flow. Since inertial forces are insignificant at low Reynolds number flows there will be little reaction when the fluid flow contacts a barrier. This is why designs for low Reynolds flow mainly revolve around creating a rotational flow to effect the mixing of the two fluids. This is accomplished by geometry such as that shown in Figure 1.8; these designs create a rotational flow that folds two entrance fluids over one another to create a greater diffusion surface area. The resulting fluid flows from these designs can be characterized as chaotic but are also predictable in the direction and speed of rotation due to the repetitive nature of the features.

This thesis will focus on the creation of a low Reynolds number design called the slanted groove design shown in Figure 1.8(a) and 1.8(b). The slanted groove mixer (SGM) was chosen for this thesis because of its simple design. Because of this the features are easily produced on the surface of the shape memory alloy. This design also shows efficient mixing making it an ideal mixer for this study.

1.4 Shape Memory Alloys

Shape memory alloys are metals that can be deformed and then returned to their original cold forged state by heating the material. Shape memory alloys work by transitioning from a rigid martensite phase to a ductile austenite phase when heated. This

is possible due to the lack of diffusions within the metal when transitioning allowing the crystalline structure to return to a distinct pattern [20].

Depending on the composition of the alloy used, the alloy will either have a one-way or two-way recovery cycle. A one-way SMA that is mechanically deformed while in its "cooled" martensite phase will return to its original undeformed shape once heated above the martensite to austenite transitional temperature. If it is cooled below the transition temperature again, it will remain in its original undeformed shape and can only be returned to a deformed state by mechanically deforming that material again. Two-way shape memory alloys have the ability to remember two shapes; one above and one below the martensite/austenite transition temperature [20]. To be able to remember both shapes the material has to be trained to do so. To train the material an external force can be applied to deform the surface of the alloy in its cold marensite state. Once heated the alloy will partially recover to its original state and partially return to its deformed state when cooled. The heating and cooling cycle can then be repeated to achieve the two shape memory effect.

SMA alloys have found many applications in academia and industry that utilize their unique ability to turn thermal energy into mechanical work. While shape memory alloys have found uses in many different industries, they are particularly popular in the aerospace and medical fields [22]. One application in the aerospace industry focuses on noise cancellation of jet engines at landing, take-off and low altitudes. This particular design uses the shape memory property to vary the nozzle diameter of the turbine. Increasing the nozzle diameter at low altitudes helps to cancel noise while decreasing the diameter at high temperatures increases engine performance (Figure 1.9). This is one of

many applications of SMA in the aerospace industry with ongoing research including airfoil optimization, noise dampening systems as well as blade actuation in rotor aircraft [22].

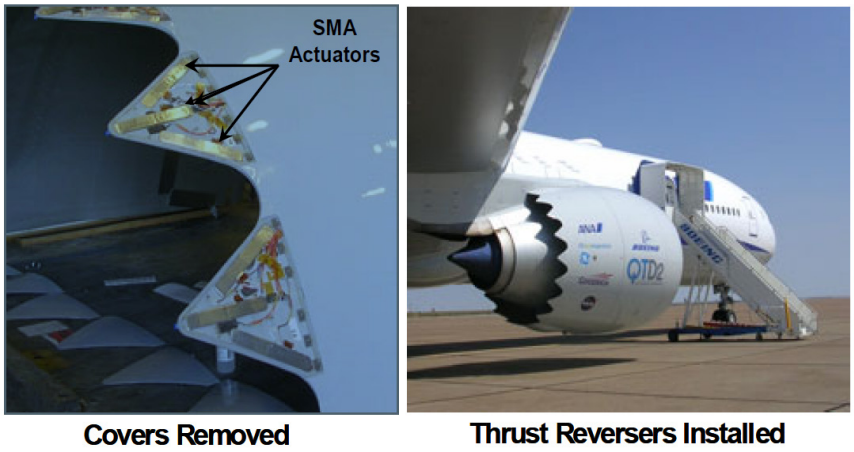

Figure 1.9: SMA actuated chevron nozzle diameter on Boeing aircraft using bulk Ti-Ni bars. Figure adapted from [23].

There are also many medical applications of SMA, despite the biocompatibility concerns associated with the most popular shape memory alloy: Ti-Ni. Current uses in the medical field include orthodontics, cardiovascular stints, as well as surgical instrumentation [21]. And although overexposure to nickel can be poisonous, it was found that any nickel that would be introduced through a Ti-Ni device would be negligible. Furthermore, the titanium in Ti-Ni devices causes a protective oxidation layer to form that retards further reactions between the alloy and the body [21].

1.4.1 Microscale SMA Features

Although SMA alloys are being increasingly utilized in industry, most applications use bulk pieces of Ti-Ni and macroscale feature sizes as compared to the microscale applications of SMA presented here. This thesis uses methods previously described by Zhang et al. [19] for the creation of microscale feature by using a

mechanical indenter to press tungsten wires into a Ti-Ni surface. This mechanical deformation is what creates the two shape memory effect showing partial or full recovery after indentation [18]. This method can also be used to create a two-way cyclic micro features that reversibly appear on a flat SMA surface when heated, as shown in Figure 1.10.

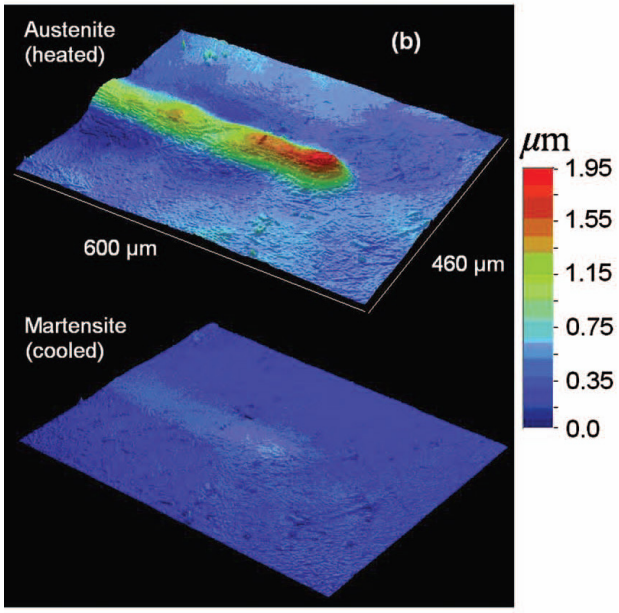

Figure 1.10: Cyclic surface protrusions on Ti-Ni surface: controlled by heating and cooling. Image adapted from [19].

This two-way effect is accomplished by introducing a planarization step after the indentation process creating a reversible transition between a flat and textured surface. Once the surface is planarized there are still areas of martensite deformation that when heated will rise up due to the internal stresses of the material present in the martensite stage. Without the presence of the internal stress in the Martensite phase the surface would remain smooth. More information on the indentation and surface characterization methods used in this thesis will be discussed in Chapter 2.

This thesis focuses on the use of SMA to create microfeatures in microfluidic devices to effect mixing. In past microfluidic studies the microfeatures in the channel that create a rotational flow are static features which create constant mixing. The goal of this study is to use a SMA surface to control the microfeatures necessary for mixing by turning them on or off using heat. This would allow mixing to be controlled by actuation of the SMA microfeatures giving the user increased control of the overall system.

Chapter 2: Computational Modeling of Micromixer

Predicting the mixing efficiency of a micromixer is challenging to do a priori, due to the complex fluid flow involved. For this reason, three different experiments were used to study the mixing efficiency of the particular device outlined in this thesis. First, a parametric study was performed using computational software (COMSOL 4.2 Multiphysics) to analyze different types of micromixer geometries. Then, a physical proof of concept study was performed to assess the viability of the proposed Ti-Ni alloy mixer as well as to discover particular flow behaviors of the microfluidic device. This study focused on creating features similar to those that would eventually be created in the shape memory alloy, and is discussed in Chapter 3. Finally a mixer utilizing the Ti-Ni SMA reversible features was integrated into a PDMS microchannel to study the viability of the complete system, as discussed in Chapter 4.

2.1 Computational Fluid Behavior Study

A finite element based physics solver (COMSOL Multiphysics) was used to evaluate the fluid flow and mixing effect of the proposed microfluidic system. Numerical simulations allow for the quick comparison of various theoretical systems in determining which system is more efficient without the time and cost of a physical experiment. This analysis also provides numbers for the comparison of the computational theoretical system to a physical microfluidic system that was created later.

When using a system that is very complex like the microfluidic device used in this study, the use of a finite element program is very advantageous in simplifying the calculation process. The physics involved—fluid dynamics governed by the Navier-

Stokes equations and chemical species transport governed by convection/diffusion equations–are too complex to derive an accurate predictive set of equations.

2.1.1 Experimental Setup: COMSOL Multiphysics

For this study, all models were first modeled in 3-D using ProE Wildfire 4.0 and exported to COMSOL. As with most CFD modules, the channel is modeled as a solid area representing the fluid within the channel to be studied. Figure 2.1 shows a representative transparent wireframe model that was imported into COMSOL for this study.

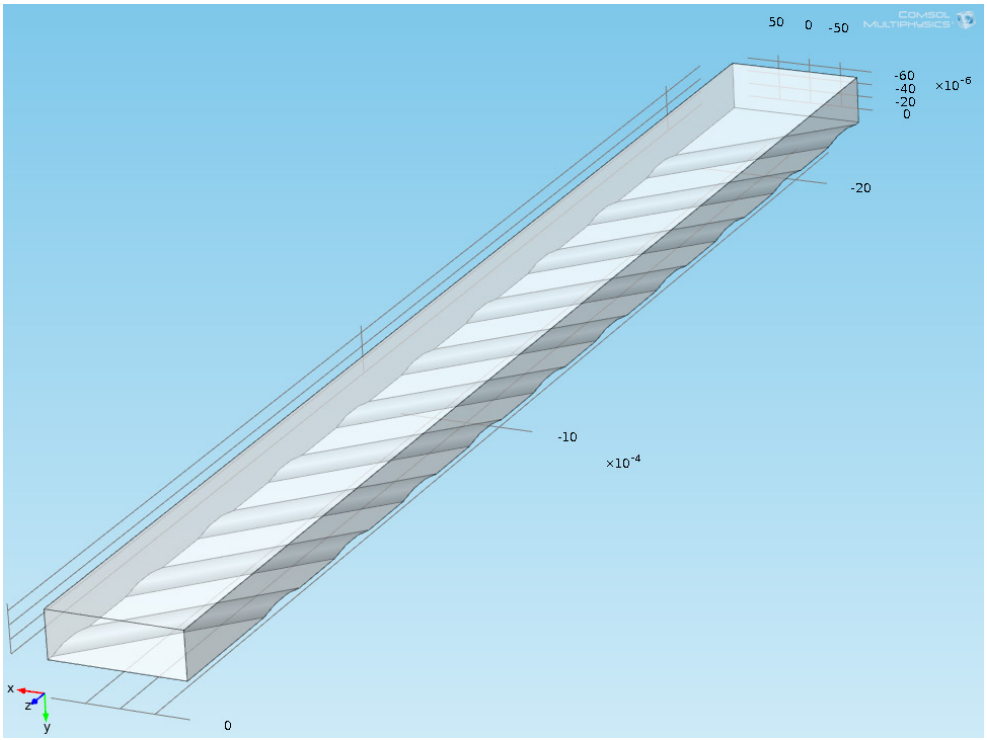

Figure 2.1: 3-D model imported to COMSOL Multiphysics.

Once the model was imported into COMSOL it was meshed for the FEM analysis. Although custom meshes can be made, the features within the program select a mesh based on the physics equations to be solved and generate a mesh. For this study, a

tetrahedral mesh was used due to small sharp corners found in the models. Depending on the model, the number of total elements varied from 80,000 to 200,000 with an average size of 8.0 μm. Figure 2.2 illustrates a typical generated mesh for the models used in this study. Due to the small size and often sharp corners in the model a tetrahedral mesh was necessary to properly mesh the entire geometry. Once the model was imported and meshed, the boundary conditions and model parameters were set in COMSOL.

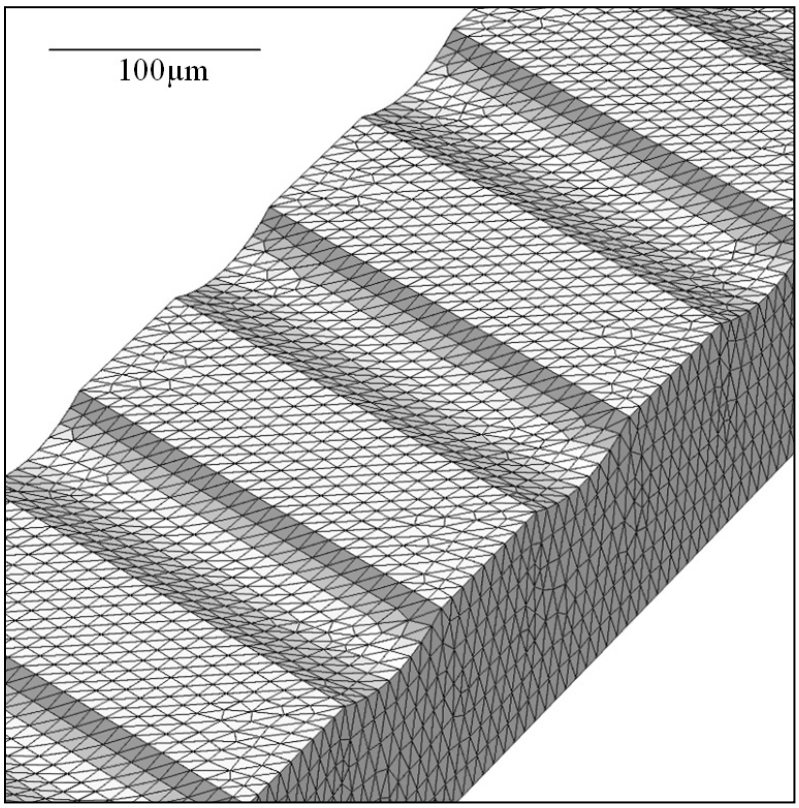

Figure 2.2: Tetrahedral mesh: Meshed microchannel with rounded features at 45 degree angle. Bottom of channel depicted.

COMSOL Multiphysics has the ability to solve multiple types of physics equations assigned to a single model simultaneously, which was advantageous for the presented system. All of the models discussed here use either the *Creeping Flow* module

to solve the Navier-Stokes equations only or both *Creeping Flow* and *Transport of Diluted Species* modules to illustrate the mixing effect between the two fluids.

The *Creeping Flow* module is used in this system for its simplification of the governing equations. As discussed in Chapter 1, the Navier-Stokes equations for microfluidic systems can be simplified into a single-phase flow by excluding the inertial terms, resulting in the Stokes flow equation (2.1):

$$\nabla p = \rho \mathbf{f} + \mu \nabla^2 \mathbf{u} \tag{2.1}$$

By applying this equation the module solves for the velocity field and pressure with the ability to add external body forces if necessary. The model conditions were set to an incompressible flow with no slip boundary conditions. All models are set to a normal inflow velocity of .03 m/s and an outlet condition of pressure equal to 0. The density (ρ) and dynamic viscosity (μ) were set to that of water: ρ=1,000 kg/m^3 and μ=0.001 Pa·s.

To model the mixing created in the microchannels through diffusion and chaotic advection, the *Transport of Diluted Species* module was used. This particular module was used due to the dilute nature of the fluids being used in the physical experiments, which were de-ionized water mixed with small amounts of fluorescent compounds for visualization. (These experiments are discussed in greater detail in Chapters 3 & 4.) When solving for diffusion, the module uses the density and viscosity of the solvent (water) for the fluid properties. This assumption is applicable since the concentration of the solvent is greater than 90 mol% of the total mixture.

Fick's law (2.2) is the governing equation for the diffusion of the dilute mixtures where J is diffusive flux (mol/m^2·s), D is the diffusion coefficient (m^2/s) and c is the concentration (mol/m^3).

$$J_i = -D_i \nabla c_i \tag{2.2}$$

Along with the convective terms a mass balance equation for species transport (2.3) can be obtained where $\boldsymbol{u}$ represents the velocity field (m/s), R is the reaction rate (mol/m^3·s) and $\frac{\partial c}{\partial t}$ is the consumption rate.

$$\frac{\partial c}{\partial t} + \boldsymbol{u} \cdot \nabla c_i = \nabla \cdot (D_i \nabla c_i) + R_i \tag{2.3}$$

When applying equation (2.3) for both fluids, no additional equation is added for the reaction term as no chemical reactions are taking place in the micromixer. Both inlet streams in this model are largely composed of water. Furthermore, the fluid flow is fully developed and stable allowing for the time dependant term to be removed which yields a simplified equation (2.4) where N is the total molar flux (mol/m^2·s).

$$N_i = D_i \nabla c_i + \boldsymbol{u} c_i \tag{2.4}$$

The diffusion coefficient for the dissolved chemical species in the model was set to D=1e-9 (m^2/s) for water. The concentration of this chemical at the rectangular entrance of the channel was split into two sections with one section set to c=1 and the

other c=0. This was accomplished by applying equation (2.5) to the inlet conditions for concentration inflow where x represents the direction of the width of the channel.

$$c = 1 \times (x < 0.0) + 0 \times (x \geq 0.0) \quad (2.5)$$

Application of these parameters gives a visual and numerical output that can be used to determine mixing quality. For these simulations the fluids are completely mixed at concentration levels of c=0.5 and considered to be completely unmixed at c=0 and c=1.

Once all parameters are set for both physics modules, the computational model was solved using time independent solvers in COMSOL. The linear system solver used was the *GMRES* solver, which is an iterative solver used for nonsymmetrical problems in fluid applications [32]. The sequence of equations was set up to solve the creeping flow module first then use the resulting velocity field to solve the transport of diluted species module. Once the solution is complete, the desired images and data sets were obtained from the solution for analysis. This general method for creating and implementing the computational model for mixing within a microchannel was used for all of the following simulations with only minor differences where noted.

2.1.2 Computational Fluid Behavior Study: Results

For our study it was desired to create a micromixer that can be turned off and on through the use of the behavior exhibited by SMA alloys. This allows for the mixer to only be used when needed and allows for the possibility of maintaining a continuously flowing system that can recycle the solute and solvent when not turned on. Because fabrication of multiple novel microsystems can be difficult and time intensive, COMSOL Multiphysics 3.5a was used to compare multiple designs quickly.

Due to physical limitations of the SMA alloy's recoverable feature size and aspect ratio, several restrictions were placed on the mixer design. A 10:1 ratio of SMA feature width to height was used based on previous findings concerning SMA cyclic features [19]. And due to the inherent complexity in fabricating complex microfeatures on an SMA surface, a simple existing mixer design (slanted-groove mixer or SGM) [5] was chosen for evaluation. Despite the simplicity of the SGM design, the dimensions of the features previously used [5] could not be reproduced due to the 10:1 width:height ratio of the Ti-Ni SMA. So in order to increase mixing efficiency, another mixer design that uses the SGM with a periodic rectangular barrier opposite to the grooves (barrier embedded mixer or BEM) was also considered [33]. Figure 2.3 illustrates both micromixer designs.

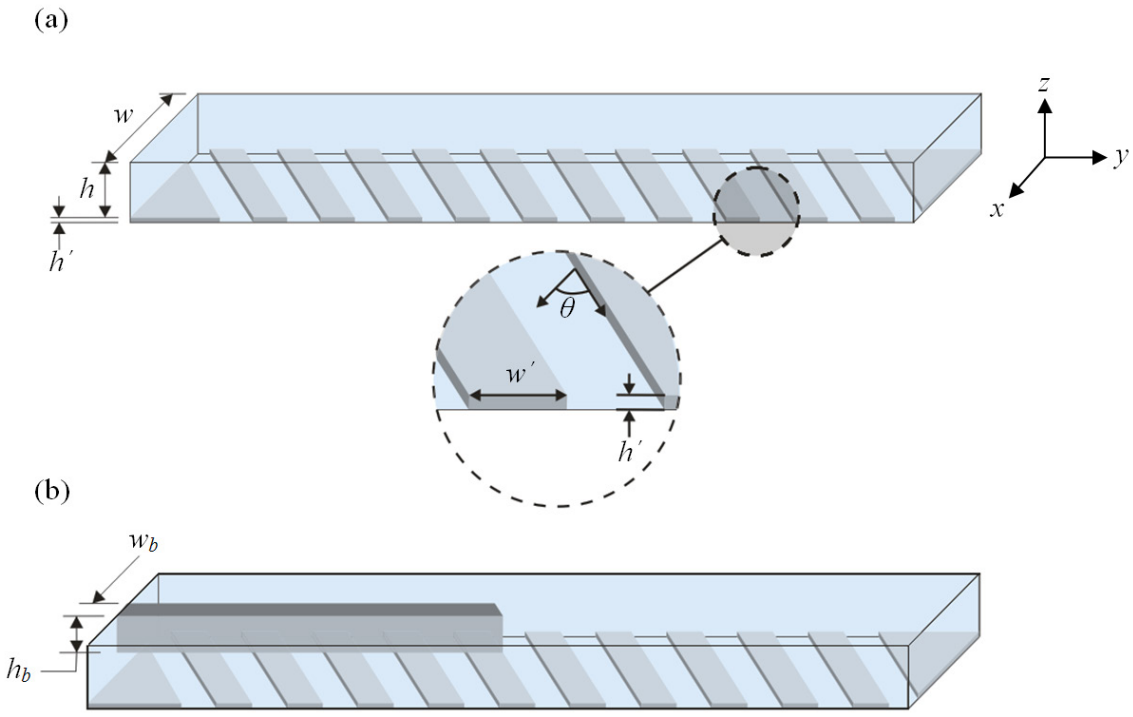

Figure 2.3: Layout and dimensions of micromixer designs: (a) SGM Design: where *h*=channel height, *w*=channel width, *h′*=feature height, *w′*=feature width and *θ*=angle of feature with respect to the positive x-axis. (b) BEM Design: where h_b=barrier height, w_b=barrier width.

For our studies, it was unknown how significant the increase in mixing would be due to the low profile (h') of our features. In addition, the barrier was a static component, meaning it impossible to be deactivated, unlike the SMA grooves. So how much effect the barrier would have on the flow in the absence of the SMA features was a point of concern. To establish the effect each feature (slanted grooves and rectangular barrier) had on the mixing efficiency of the system, four microchannels were modeled. The four channel designs consisted of the following: (1) Slanted Groove Only (SGM); (2) Embedded Barrier with Slanted Grooves (BEM); (3) Embedded Barrier with no Slanted Grooves (Periodic Barrier); (4) featureless rectangular control channel (Empty Channel).

The BEM is similar to the SGM except for an added rectangular barrier opposite from the grooved features for half of one cycle. Both mixers use the principal of chaotic advection discussed in Section 1.4. Chaotic advection is induced through a rotational flow created by the slanted grooves. The main difference between the SGM and BEM is the presence of two areas of rotation present in the BEM model as shown in Figure 2.4. An increase in mixing efficiency has already been shown in past studies when using the BEM over the SGM [33]. But these studies incorporated slanted features that were spaced closer together with larger heights. Due to the change in geometry of the slanted features it was unknown whether the barrier would significantly contribute to mixing efficiency.

Due to the periodic nature of the channel, the geometry was sectioned into consecutive cycles which allows for faster computational times. Figure 2.3 illustrates one cycle which includes 10 grooved features. To simulate a longer channel, the exit

concentration of each cycle was mapped back to the entrance for the next simulation. Due to the limitations of the software, the velocity fields could not be mapped back to the entrance as well. This resulted in the velocity field of each channel starting over at the initial conditions. Because of this, the following results are considered to be qualitative data sets for comparison of the four micromixer types and not quantitative data sets to be compared with experimental results.

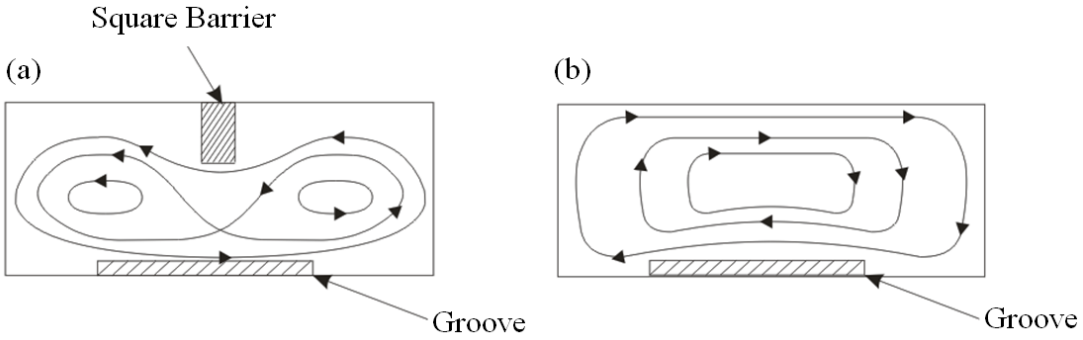

Figure 2.4: Cross-section view of channel, xz plane: (a) SGM-Rotational Flow with single vortice, (b) BEM-Rotational Flow with two vortices. Figure adapted from [33]

For comparison of the effectiveness four micromixer types all variables were held constant except for the feature geometries. For this particular study the critical dimensions are as follows for all channels: w=200µm, h=77µm, w'=100µm, h'=7µm, θ=45°, w_b=30µm, h_b=40µm. Inflow was uniform at 0.03 m/s with no slip boundary conditions. At the end of each simulation the concentration profile image was exported as well as the data file. This allowed for a side by side comparison of the concentrations profiles of the various geometric configurations. Figure 2.5 illustrates the channel geometry and concentration profiles of the first cycle for each of the four micromixer types.

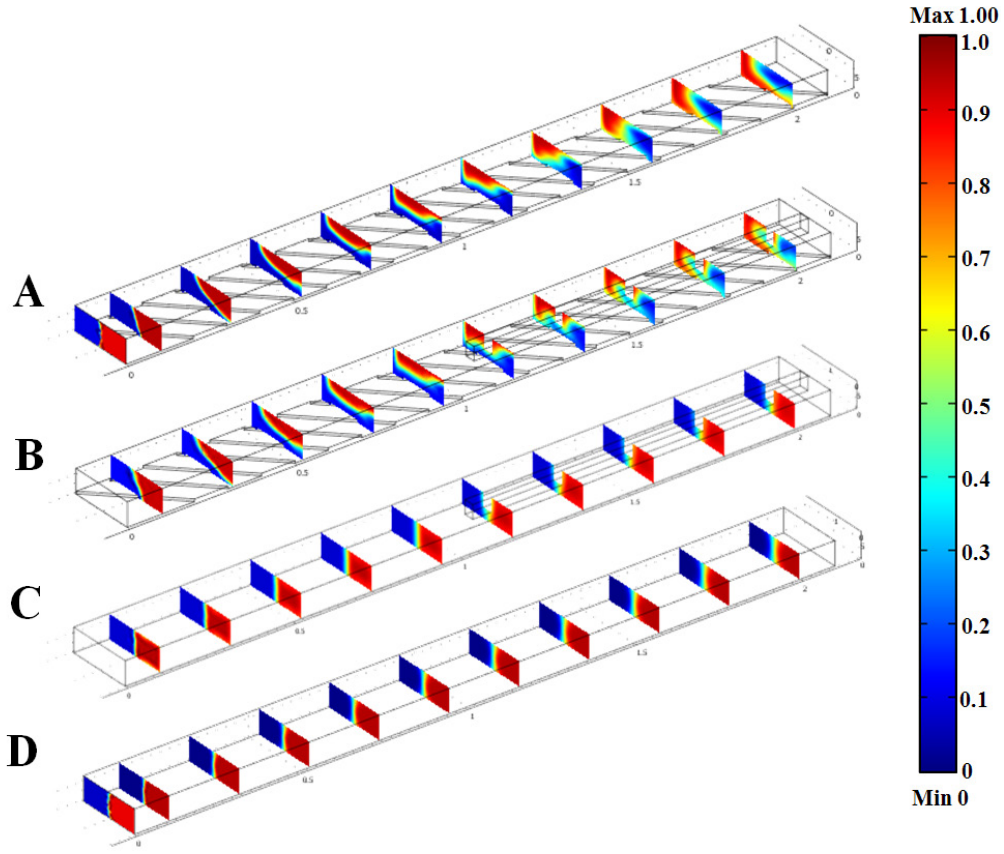

Figure 2.5: Concentration profiles of 1st cycle of varying microchannel geometries: (A) Slanted Groove Method-SGM, (B) Barrier Embedded Method-BEM, (C) Periodic Barrier, (D) Empty Channel.

In addition to image comparison MATLAB R2009a was used to calculate the percentage mixed of each profile with a concentration of 0.5 being 100% mixed. Figure 2.6 shows the cross-sectional concentration maps and comparisons of mixing efficiency at different positions along the microchannels.

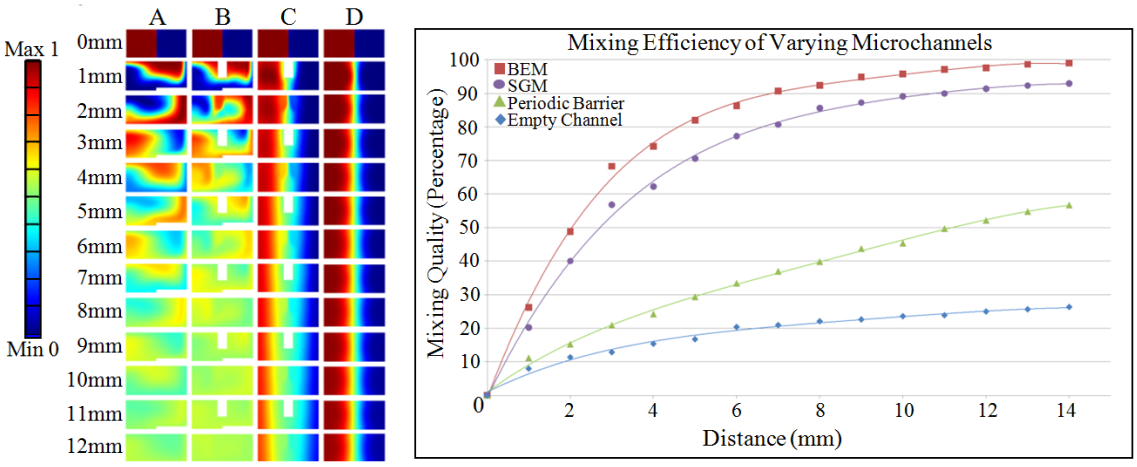

Figure 2.6: Cross-sectional concentration profiles of geometries A, B, C, and D (left). Comparison of mixing quality vs. distance from inlet for SGM (A), BEM (B), Periodic Barrier (C), and Empty Channel (D) (right).

As expected, each micromixer geometry affects the flow in a distinctive way that in turn creates unique concentration profiles. The SGM geometry (A) and BEM geometry (B) both exhibit a rotational flow while BEM shows an increased mixing effect over the SGM. This is can also be seen in the graph in Figure 2.6, as calculations of BEM efficiency show an 8.25% average increase in mixing quality over SGM. In contrast to the rotational flows in A and B, the Periodic Barrier (C) and Empty Channel (D) geometries exhibit laminar non-chaotic flow except for minor disturbances created by the barrier in channel C. The addition of the barrier in channel C has a significant effect on the mixing quality of the channel resulting in an average increase of 17% over channel D.

Although the BEM method showed an increase in mixing quality over the SGM method, the barrier by itself showed that it had too much of an influence on mixing to use the BEM method. In order to be able to recycle the solvent and solute at the end of the

channel, the two fluids must mix or diffuse across the channel as little as possible. Due to the large increase in mixing in channel C over channel D, the BEM method was ruled out as a possible design, and the SGM method was used. Since the gain in mixing quality from channel B to A was only approximately one half of the gain from D to C, the choice to not use BEM will have a minimal impact on mixing quality in the actuated state.

Once the SGM was selected to be the basis for the mixer design, additional simulations were completed to study to rotational velocity field created by the slanted grooves. To obtain an accurate simulation, the limitations of the SMA features previously discussed were taken into account. This required the slanted grooves to be modeled with rounded edges which more closely resembled the profiles previously demonstrated in Ti-Ni (Figure 2.7) [19].

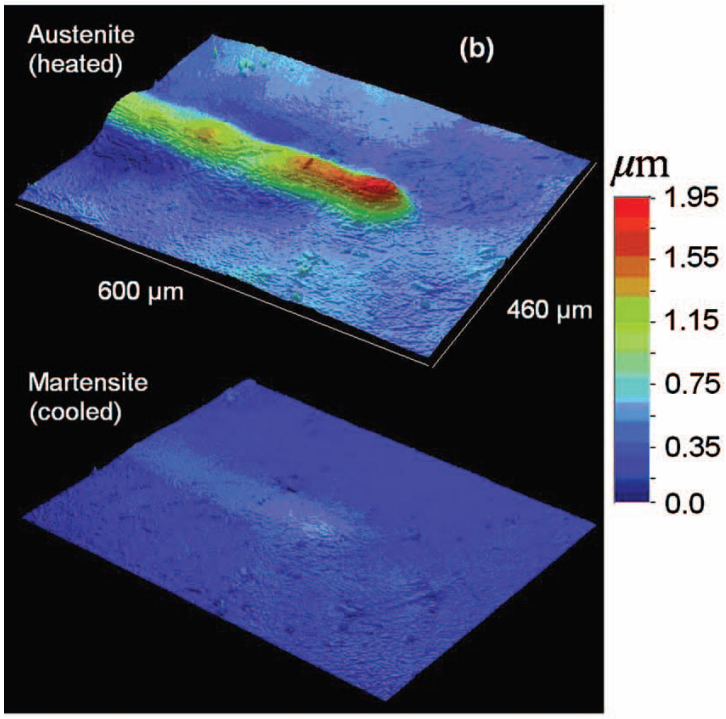

Figure 2.7: White light profilometer image of microfeature: Created in Ti-Ni SMA surface. Adapted from [19].

This limitation along with the previously discussed 10:1 width to height ratio led to the redesigned feature profile shown in Figure 2.8.

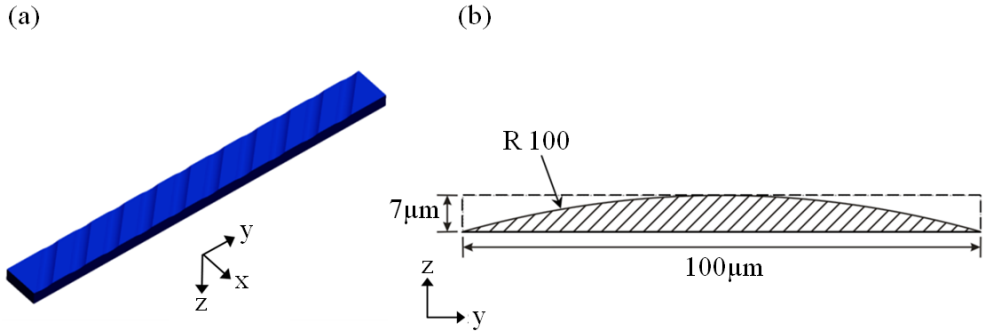

Figure 2.8: (a) 3-D representation of interior volume, single cycle with rounded features. (b) Rounded feature profile view where *h*′=7 µm and *w*′=100 µm.

Again, the finite-element software package COMSOL Multiphysics was used to simulate the fluid flow by solving only for the Navier-Stokes equations over the

generated mesh. For this simulation, an inlet velocity of 3 cm/s was used along with the *Creeping Flow* module of COMSOL. Cross-sectional profiles of x and z velocity fields were taken at the middle of the 10th feature. The resulting data sets were analyzed using MATLAB to create Figure 2.9.

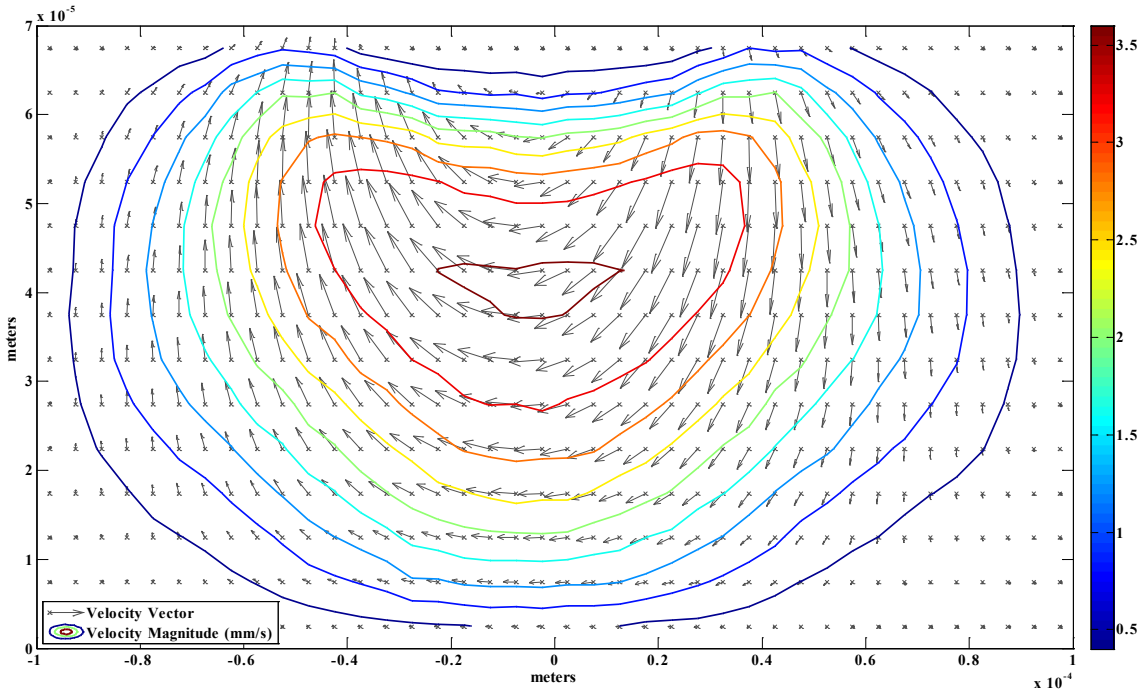

Figure 2.9: X and Y cross-sectional velocity vector and magnitude plot. Taken at 10th feature of 1st cycle. Image is oriented with the SMA feature at the top of the image.

A rotational flow is evident in the plot above that was induced by the slanted feature at the top of the channel. The presence of the greatest velocity magnitudes and directional changes in the areas directly above and surrounding the feature illustrates the affect of the feature on the rotational flow. This rotational flow was built upon by each successive feature creating a uni-directional chaotic flow that contributed to the folding of the two fluids being mixed. The observed rotational flow in this plot was not present

in a featureless channel, which caused minimal mixing of the fluids in the absence of the SGM.

The vorticity map shown in Figure 2.10 also illustrates the increased tendency for rotation in a SGM channel over a featureless channel. The cross-section of the SGM microchannel (b) shows a 29% increase in vorticity over the Empty Channel (a); this effect is concentrated on the top and bottom of the channel. Plot (b) also shows that the area of greatest vorticity occurs at the fluid-feature interface.

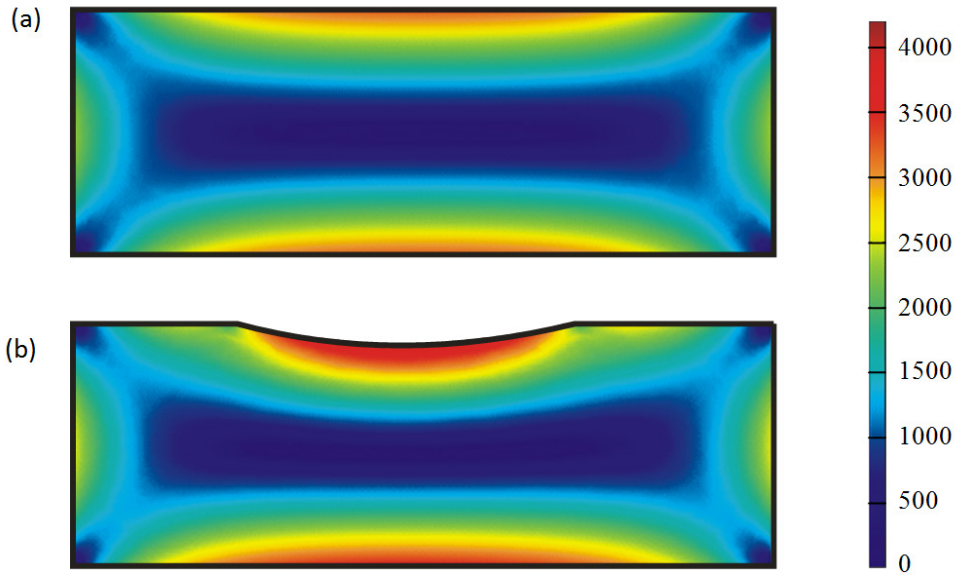

Figure 2.10: Vorticity Magnitude (1/s): (a) Vorticity cross-section of empty rectangular channel, max=3206; min=44. (b) Vorticity cross section middle of 10th feature in 1st cycle, max=4129; min=29. Channel is oriented with SMA feature on the top of the image.

A significant rotational effect from the features can be observed despite the added restrictions imposed on the feature geometry by the use of SMA. To obtain an idea of how much the rotational velocity field affects the contact surface between the two fluids, a chemical species transport can be added to the simulation. Figure 2.11 below shows the concentration profiles from the entrance of the channel and the profile after the 1st cycle

or tenth feature. To obtain a numerical value for the increased contact surface area, the profiles were edited to exclude any diffusion that occurred between the two fluids and only show the interface line between the two fluids.

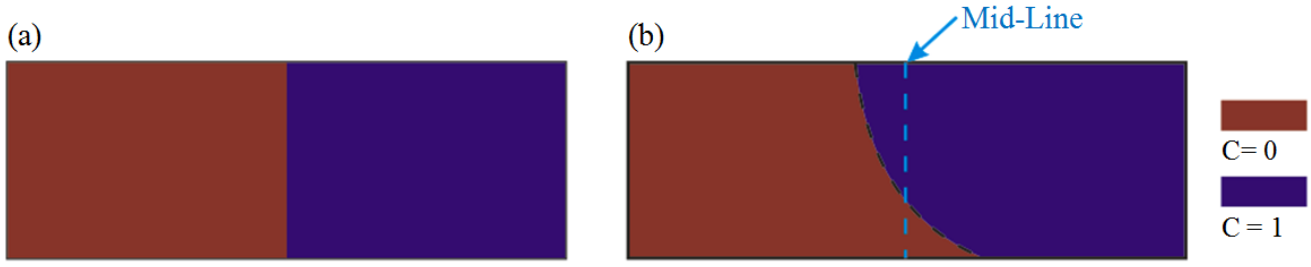

Figure 2.11: Concentration Profiles: (a) profile at channel entrance (b) profile at end of 1st cycle (10 features).

The contact surface area for diffusion from a to b increased by 26% from 70 µm to 88.3 µm while shifting the fluid interface on the bottom by 27 µm and the top by 19 µm. This shows that the fluid tends to rotate counterclockwise. The features are oriented on a 45° angle to the direction of the flow and start on the left side and move to the right. This corresponds to the fluids tendency to move to right along with the features.

After initial FEM software models, the SGM was determined to be the most well suited mixer design for use with the desired applications using a SMA surface. Further models of the SGM showed the designs ability to effect a rotational flow from otherwise laminar flow when in a featureless channel. Within the SGM model, the area of greatest rotation or vorticity tends to be directly above and around the slanted features with a tendency to flow across the channel in the direction that coincides with the direction of the features. In conclusion, these models and results support the viability of the SMA micromixer design and concept put forth in this paper.

Chapter 3: PDMS Proof-of-Concept Experiments

In order to demonstrate the validity of the micromixer geometry before fabricating the SMA component, a proof-of-concept physical model was made and tested. This model was fabricated entirely from an elastomer: polydimethylsiloxane (PDMS), so the mixing features could not be turned "on" and "off", but it enabled experimental observation of the flow path that could be expected from the SMA system.

To build an accurate proof of concept physical model the micromixer was fabricated as closely as possible to the specifications of the proposed SMA model. Several limiting factors to the complexity of micromixer arose due to the properties and behavior of the SMA features, as previously discussed in section 2.1. SMA features are limited to a 10:1 width to height ratio, this allows for the height of the feature to only be one tenth of the smallest nominal dimension of the footprint of the feature [19]. Fabrication methods used in this study also limited the capabilities to produce complex features on the SMA surface due to the difficulties of working on the micrometer scale. For this reason the SGM model which uses only straight-line features was chosen over more complex geometries such as the staggered herringbone design that consists of v shaped features.

3.1 Fabrication Methods

There are many microfabrication methods that are currently used for the production of microstructures including CMOS processing techniques, laser machining, and electrical discharge machining and traditional precision milling. A key step in most CMOS processing techniques is the use of photolithography, which is used to transfer of

a pattern onto a substrate through the use of photosensitive chemicals. These steps can be followed with etching or material deposition steps to add or subtract material, respectively.

Photolithography is one method that is widely used in the production of microscale features for MEMS and microfluidics applications. In this method, a pattern is transferred to a substrate through optical means; in this case a ultra-violet light source is used to transfer the desired pattern. To achieve this, a photosensitive polymer of controlled thickness is deposited by spin-coating a surface. After coating the wafer a mask is placed on top and the material is exposed through the patterned mask. Once exposed the resist is heat treated and immersed in a bath of resist stripper that removes all unexposed areas. This method of photolithography is capable of fabricating features with submicron pattern fidelity. Since the smallest critical dimension found in the microchannels used in this study is 70 μm, photolithography was found to be a suitable step in the fabrication process.

Etching works only through the removal of material via exposure of a substrate to a liquid or gas that will selectively dissolve a particular material. If material deposition is required, there are a wide range of physical and chemical vapor deposition techniques that deposit or add the material onto the substrate to create the desired features [24]. Chemical vapor deposition coats one or more chemicals onto a substrate in the desired pattern. Once deposited the chemicals will react or decompose on the substrate creating the desired features. Sputter deposition works in a similar manner but adds material by using an ion beam to bombard a metal target which strips ions off the target and deposits them onto the substrate. E-beam evaporation is similar to sputter coating except for the

use of a target anode that is converted to vapor form through bombardment of an electron beam. The resulting vaporized material deposits a thin film onto the substrate [24].

Photo and soft lithography techniques are the methods used for micro fabrication in this research. Soft lithography is the fabrication or replication of a stricter through the use of elastomeric materials [24]. Soft lithography is advantageous because of its ease of manufacturing, high pattern fidelity and low cost. To fabricate a micromixer an elastomer is used to mold a channel from the photolithography master. This results in channel in the elastomer that has three walls. To seal the channel a glass slide is permanently bonded to the elastomer through plasma bonding. This process creates a permanent seal between the two materials.

3.1.1 SU-8 Mold Fabrication Process

To start the process a silicon wafer was vacuum sealed to the chuck of a spin coater. Next, SU-8 photoresist (Microchem) was poured onto the center of the wafer and evenly spread over the wafer through spin coating. A spinning time of 30-45 seconds was used to allow all excess resist to be removed resulting in a uniform film of the desired thickness on the wafer. The wafer was then baked at 95°C on a hot plate for 5-15 minutes depending on thickness to remove excess solvents in the solution creating a rigid resist layer.

After cooling the wafer to room temperature, it was placed into a mask alignment machine along with a patterned chrome photomask. After aligning the pattern of the photomask to the wafer, the two were brought into contact and exposed to an ultra-violet light source. The wafer was then removed from the mask aligner and subjected to a post-

exposure baking step for 3-15 minutes based on thickness at 95°C. The SU-8 was permanently cross-linked anywhere it was exposed to the light source after the post-bake. If only a single layer of SU-8 was desired, the un-exposed resist was dissolved off the wafer using a chemical developer solution (Microchem).

To create more complex molds, like the majority of those used in this thesis, a slightly modified version of the steps outlined above were repeated to create microstructures consisting of two layers of resist. The complexity of the desired features is only restricted by the number of layers used and the unidirectional exposing process. The two step process used is illustrated in Figure 3.1 and detailed in Appendix A.

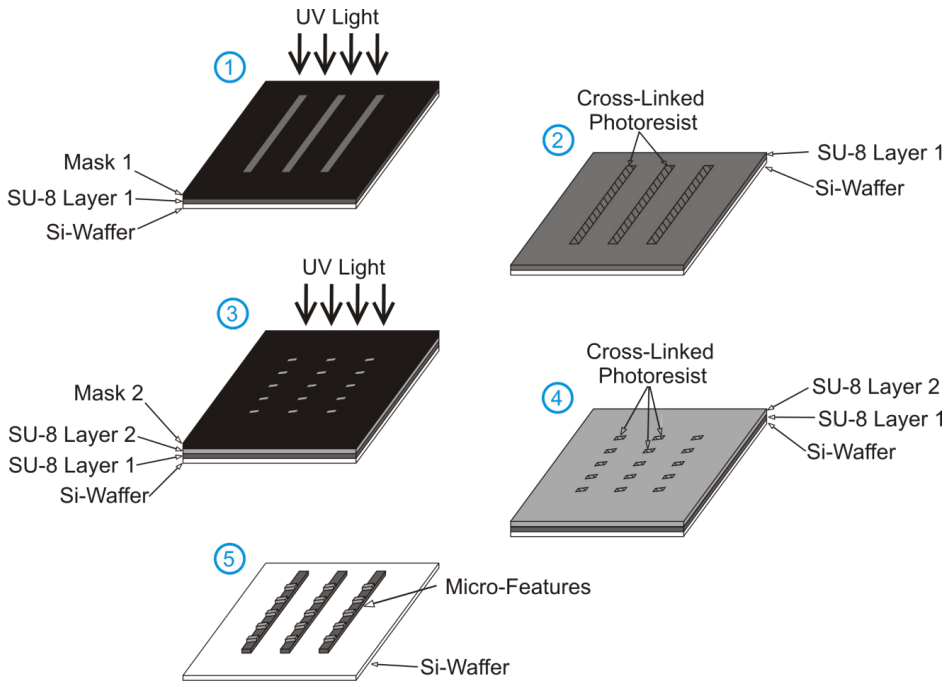

Figure 3.1: Two layer photolithography process: (1) SU-8 coated wafer is exposed to UV light with the photomask for the first layer on top of the SU-8. (2) Mask 1 is removed and first layer photoresist is cross-linked in desired areas. (3) Second layer of SU-8 is applied and exposed to UV light with second layer photomask on top. (4) Mask 2 is removed and second layer photoresist is cross-linked in desired areas. (5) All photoresist not cross-linked is removed with developer solution resulting in the formation of the desired microfeatures.

Due to the small size of the fabricated features, concerns that would be inconsequential on a macro scale can lead to defects on the micro scale. For this reason, all fabrication is done in a clean room to avoid any dust or debris from contaminating the sample that could produce defects if present. It is also important to be very careful during the SU-8 spinning step in the microfabrication process since any defects created in this step can be transferred to the final microstructures. Defects such as bubbles in the liquid SU-8 can greatly affect the flow properties of the resist, which can alter the final dimensions of the structure. Because of this it is important to properly prepare the surface of the wafer as well as correctly pour the resist onto the wafer. Even the age of the photoresist used can alter flow properties and change the resulting height of the fabricated features.

3.1.2 SU-8 Characteristics and Flow Properties

The photoresists used in this research were from the SU-8 3000 series manufactured by Microchem. SU-8 3000 is an epoxy based negative photoresist that is used in a variety of MEMS applications with thicknesses varying from 4 to 120 micrometers. SU-8 is capable of producing micro structures with aspect ratios as high as 5:1 [25]. Since the resist is negative it becomes permanently cross-linked anywhere it is exposed to a UV-light source. Negative resist also exhibits excellent adhesion to silicon, and is not susceptible to over developing due to its excellent wet chemical resistance [24].

To control the thickness of the micro features, multiple resists with varying viscosities were spun at varying rotational speeds in accordance with the specifications of the particular resist. Film thickness depends on rotational speed, concentration of the

resist and the viscosity of the resist. A first layer thickness of 70 µm and second layer thickness of 7 µm were desired. To accomplish, this SU-8 3050 and SU-8 3005 with thickness ranges of 45-100 µm and 5-10 µm, respectively, were used. Spin speeds were taken from the chart shown below that illustrates the spin speed to thickness ratio of SU-3000 resists.

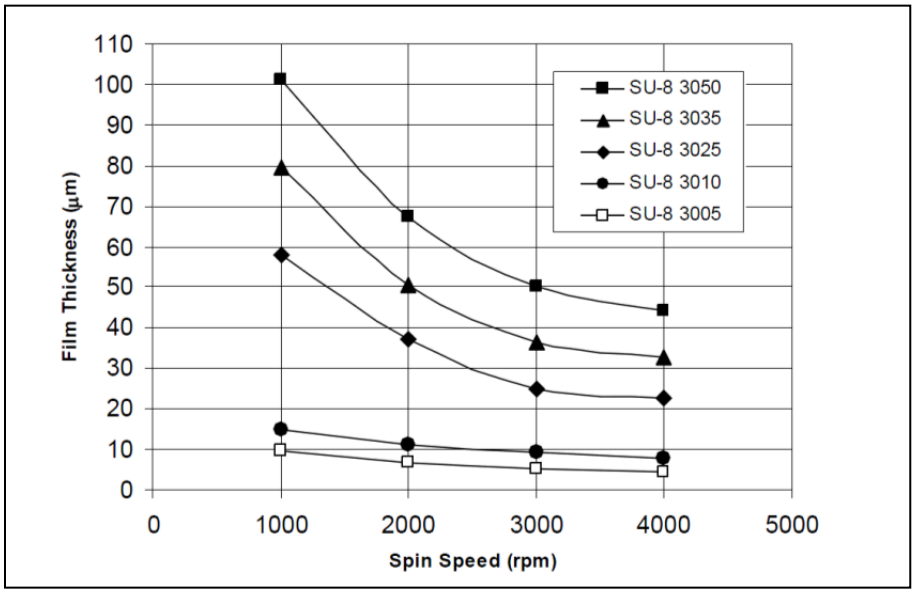

Figure 3.2: SU-8 3000: Spin Speed to Thickness Ratio. Figure adapted from [25].

Although the spin speed to thickness relationship followed the general trends in the above chart, the actual thickness of the SU-8 resist varied from the chart. When creating a two-layer mold as described in the previous section, the first layer of photoresist was easily controlled to achieve a uniform layer of the desired thickness; however it was necessary to increase the spinning speeds and times to achieve the desired thickness. Since the second layer of resist was spun on top of the first layer of resist and not a silicon surface, the speed to thickness ratio in the above table did not hold true due to an interaction between the two layers of resist. This was observed in an experiment where a layer of SU-8 3050 was spun at 6,000 rpm on top of the first layer of resist as

well as a blank silicon wafer holding all other parameters constant. A difference in height of 6.5 μm was found with the average height of the resist and silicon surfaces were 10 μm and 3.5 μm respectively.

To achieve the desired height of approximately 7 μm on the second layer, the SU-8 3005 resist had to be diluted to decrease the viscosity of the solution. The table below details the viscosity of the SU-3000 resists. Dilutions ratios of 1:2, 1:1 and 2:1 of SU-8 thinner and SU-8 3005 respectively, were prepared and spun as the second resist layer. It was found that any dilution ratio of 2:1 or higher resulted in a non-uniform layer that was inadequate as a mold surface. An equal 1:1 dilution yielded a uniform second layer with an average height of 9.5 μm. Since the height of the channel created by the first resist layer is sufficiently larger than the desired and fabricated height of the second layer, 7.0 μm and 8.5–10.5 μm respectively, the fabricated second layer was deemed adequate for proof of concept experimentation.

Due to the large number of factors that influence on the final height and quality of the spun resist, the ideal processing parameters had to be determined experimentally. Several factors including spin speed, spin time, volume dispensed, resist age, spinning program, and resist concentration were varied to achieve the final desired wafer. Overall, spin speed, resist age and quality of the pour onto the wafer were found to have the greatest influence on the resulting resist layer. Appendix A includes the details of these parameters with the final achieved thickness.

Table 3.1: SU-8 3000 Series Viscosity. Figure adapted from [25].

SU-8 3000	% Solids	Viscosity (cSt)	Density (g/ml)
3005	50	65	1.075
3010	60.4	340	1.106
3025	72.3	4400	1.143
3035	74.4	7400	1.147
3050	75.5	12000	1.153

3.1.3 Photomask Production

A mask for photolithography can be fabricated by a number of methods. The chrome on glass masks used in this research were created using a direct write system at the University of Louisville. Masks can also be produced with methods as simple as printing the desired pattern onto a transparency. But when creating features on a very small scale, the use of a transparency mask is limited by the resolution of the printer, and most commercial printers do not have high enough resolution to create quality microscale features. In addition, the layer of ink used to print the pattern cannot guarantee that there will be no light transmission through the printed areas. Chrome masks guarantee no light transmission through the printed surface and can easily obtain microscale feature sizes.

Figure 3.3 shows an optical micrograph of the boundary of the chrome surface on one of the chrome photomasks used in this research. The areas of chrome printing are shown in black and the exposed area of the mask in white–these are the areas where the SU-8 photoresist will permanently cross-link. The resolution of the photomask printing process is very high, although small fillets can be seen in the bottom corners of the exposed area where the corners should be sharp. This was most likely due to the minimum pixel size of the chrome direct write system. Since the rounding on the corners

(1.2µm) was much smaller than the overall dimensions, any affect the changed geometry had on the system was assumed to be negligible.

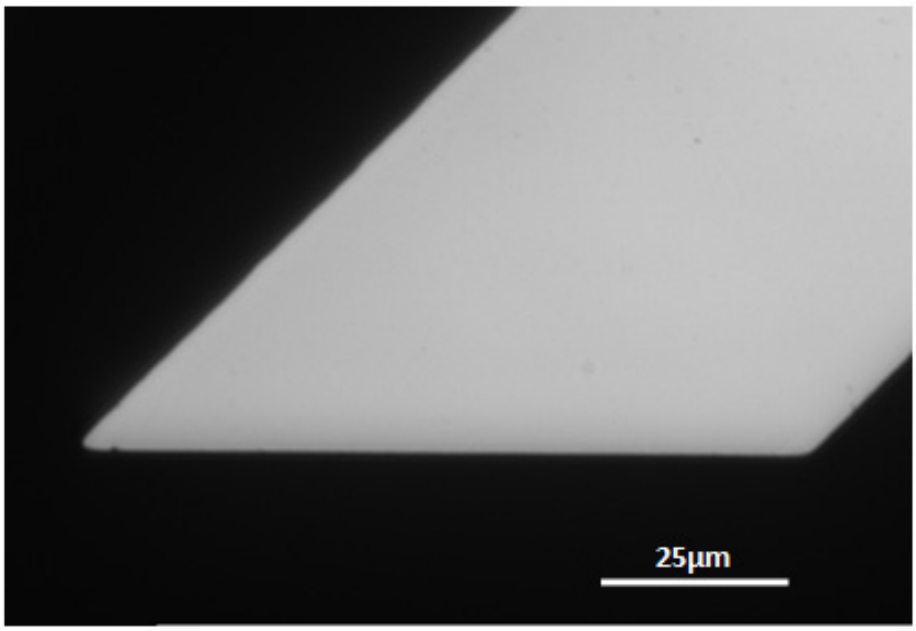

Figure 3.3: Optical micrograph of the chrome boundary of the photomask; chrome areas shown in black.

3.1.4 Microchannel Molding

Traditional methods for fabrication of microfluidic devices involves the use of silicon and glass surfaces with similar photolithography procedures from above but also often include steps of chemical etching and/or material deposition. These methods require the removal of material from the silicon or glass substrate to form a three dimensional channel. When using chemical etching, the desired pattern is developed in a layer of photoresist exposing the silicon or glass substrate in the areas to be etched. Then the sample is exposed to a chemical, often an acid, to etch the areas of exposed substrate. This process works on the principle that the glass or silicon will react with the acid while

the photoresist will not. After the etching process is complete, the photoresist is chemically removed, resulting in the microfeature etched into the surface of the substrate. Chemical etching and other similar methods can often be time intensive and costly. These processes often lead to microstructures that have inconsistent dimensions and are of limited complexity [26].

Alternatively, organic polymers have been increasingly used to create high fidelity microchannels quickly and cheaply. Such organic polymers often come in a liquid form and can be cast to a desired surface using a curing agent. PDMS (Polydimethylsiloxane) has become an increasingly popular silicon polymer used for microfluidic applications.

Several characteristics of PDMS make the fabrication of microfluidic devices quick, simple and inexpensive as compared to traditional methods. PDMS has the ability to conform to very small geometries allowing for the creation of high accuracy molds. PDMS is transparent optically when cured into its final state, which greatly simplifies the imaging process. Also, curing times can be controlled by lowering or raising the ambient temperature resulting in curing times from 10 minutes to a full day. After curing the resulting material is a flexible silicon rubber that is durable and easy to manipulate. Furthermore, the elasticity of the material can be manipulated by increasing or decreasing the curing to base mixing ratio which raises or lowers the Young's Modulus of the cured PDMS. Finally, oxygen or air plasma can be used to easily bond PDMS to any glass surface. All of these characteristics make PDMS an ideal material for the fabrication of a microfluidic device.

The surfaces generated through photolithography methods function as positive master molds that represent the interior of desired microfluidic channels. Since cured SU-8 is permanently cross-linked and is thermally stable the geometry of the channel on the silicon wafer can be repeatedly used to cast negatives of the master mold in PDMS without considerable wear to the microstructures [24]. The resulting PDMS mold is a microchannel recessed into the surface of the material. Figure 3.4 illustrates the principle of the PDMS channels being molded from the master SU-8 mold.

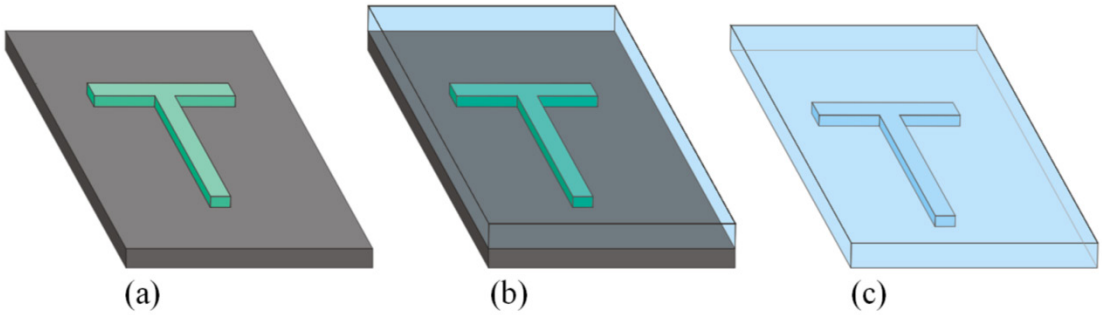

Figure 3.4: Illustration of PDMS molding process: (a) an SU-8 positive master mold on a silicon wafer, (b) liquid PDMS is poured onto master mold during the molding step, (c) after thermally curing, the PDMS negative of the SU-8 is removed from the mold.

The molding step shown in Figure 3.4(b) was achieved by cutting a circular gasket from a 4.5 mm thick piece of acrylic and attaching it to the silicon wafer as depicted in Figure 3.5. Next the PDMS (Sylgard 184, Dow Chemical) was prepared by mixing the liquid base component with the curing agent in a 10:1 ratio. Once the PDMS was mixed and degassed in a vacuum chamber for 30 minutes, it was poured into the mold and thermally cured in an oven. Curing time was dependant on the oven temperature; with a temperature of 100°C, the PDMS would completely cure in 10 minutes. After curing, the PDMS was removed from the mold and cut into desired dimensions.

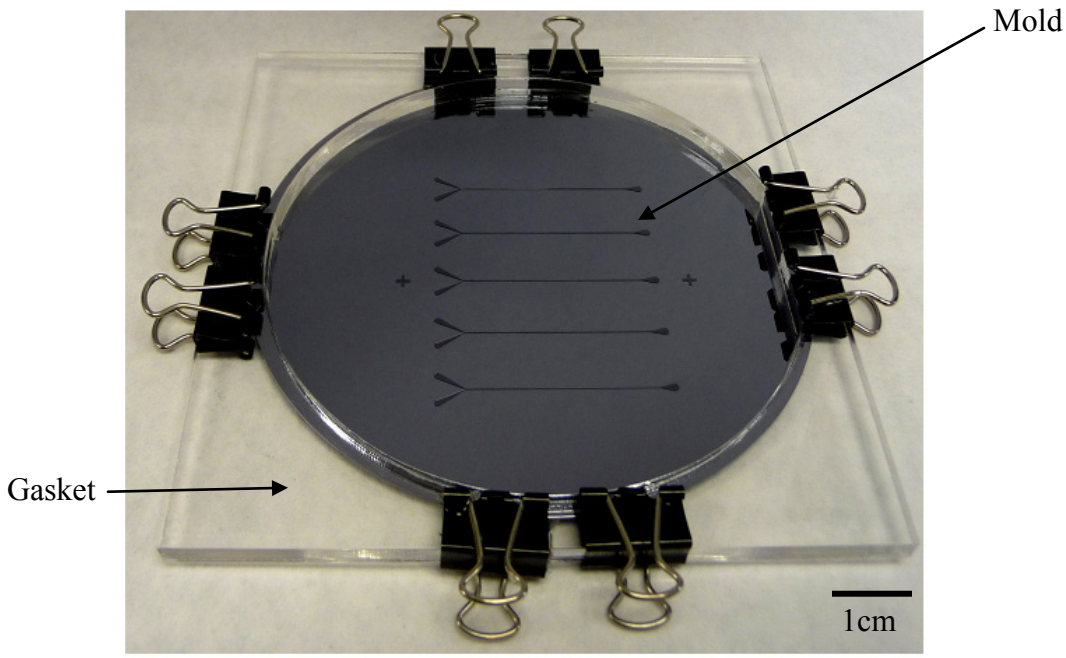

Figure 3.5: SU-8 / Si wafer mold and acrylic gasket assembly filled with liquid PDMS.

As previously discussed, PDMS shows a very high pattern fidelity when dealing with microscale dimensions. Once cured, the PDMS channels closely mimic the SU-8 microfabricated features of the original mold. Figure 3.6 shows on optical micrograph of the patterned PDMS microchannels generated from the SU-8 mold.

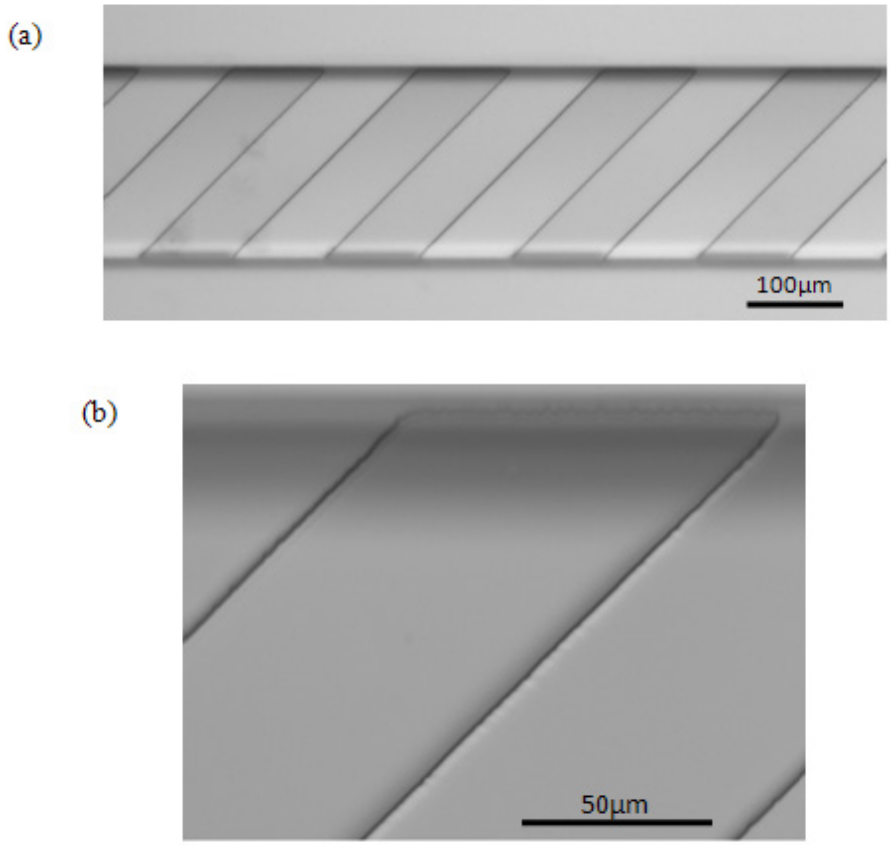

Figure 3.6: Patterned features of PDMS microchannels at 10x (a) and 40x (b) magnification.

The patterned features in the cured PDMS closely mimicked the features on the silicon wafer. A small curvature in the corners of the feature can be seen in Figure 3.6 (b). This rounding effect is not a result of the PDMS casting process, but rather the resolution of the photomask previously discussed as well as the photolithography process. Such a small deviation from the original design of sharp corners will not have a significant effect on the overall system. After curing is complete and the pattern has been successfully transferred to the PDMS, the mixers can be bonded to enclose the channel and complete the system.

3.1.5 Channel Bonding

After the molding process was complete, three of the four sides of the channel were formed in the PDMS components. From here the channel had to be enclosed by adding a fourth wall in order to make a viable channel for fluid flow. Inlet and outlet ports in the system were also created to be able to inject fluid into the system and create a steady uni-directional fluid flow. Inlet and outlet ports were formed by using a blunt needle (luer stub) to punch a hole to the channel from the opposite surface of the PDMS, as illustrated in Figure 3.7.

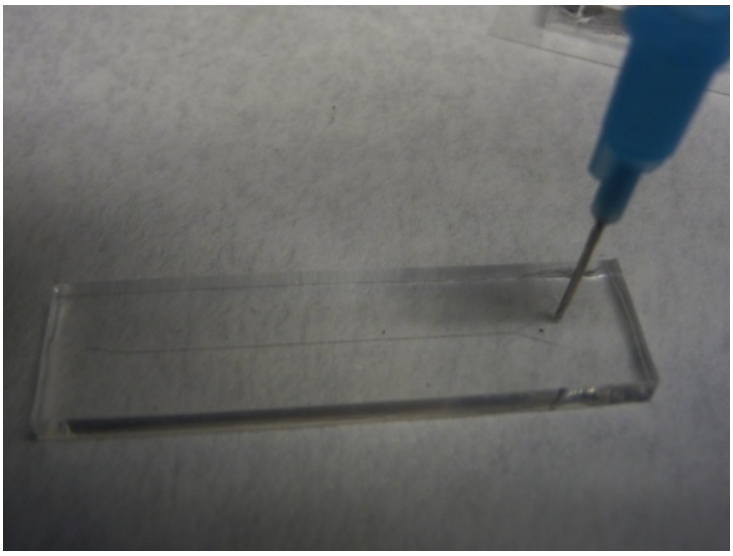

Figure 3.7: Inlet/Outlet port creation in PDMS device using blunt luer stub.

Once the entrance and exit paths are created, the channel was enclosed with a glass microscope slide acting as the fourth wall. This was done by exposing the surfaces of the glass and PDMS that would be bonded together to oxygen plasma. This action alters the surface of the PDMS and the glass that allows for permanent adhesion when

these two surfaces are brought into contact with each other. Initial adhesion is instantaneous and becomes permanent, resulting in an irreversible bond between the PDMS and the glass slide. The resulting microchannel is depicted below in Figure 3.8.

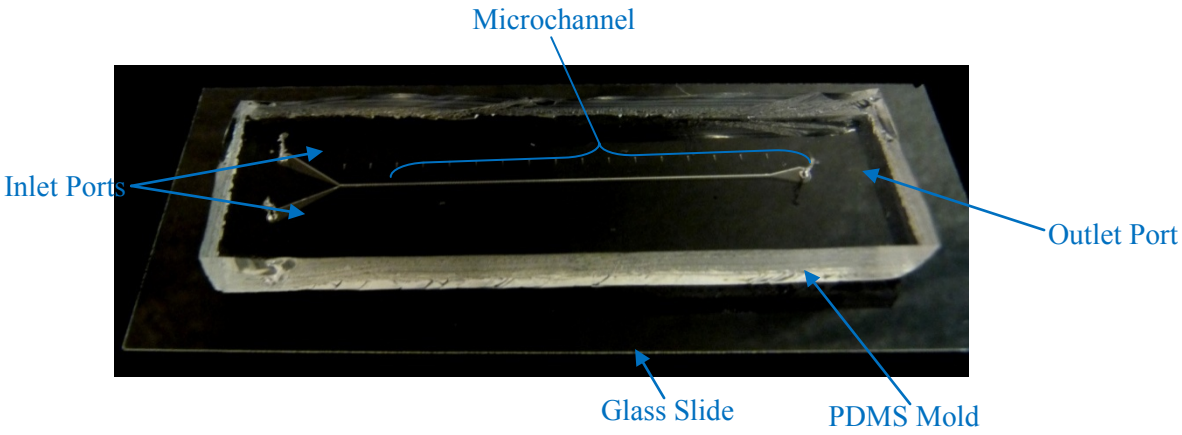

Figure 3.8: Fabricated PDMS microchannel mounted on glass slide. The approximate channel length is 33 mm.

The quality of the bond depends on the type of plasma used and exposure time, with over exposure leading to decreased adhesion. These parameters were addressed in the adhesion process detailed in Appendix B.

3.2 Experimental Setup

In microfluidic systems, the fluid flow can be influenced by even minor external forces or changes in the system components. Because of this, extra care was taken with the experimental setup to achieve a stable microfluidic system. The main components of the system consisted of a screw operated dual syringe pump, two 1 mL Slip Tip syringes, silicone tubing, and luer stubs and metal connectors for fluid transport to and from the micro channel. Specifications for the tubing, luer stubs, and connectors are shown in Table 3.2.

Table 3.2: Component Specifications: luer stubs, connectors and tubing.

Component Specifications		
Component	Inner Diameter (mm)	Outer Diameter (mm)
Luer Stub	0.41	0.71
Connector	0.41	0.71
Silicone Tubing	0.64	1.19

The larger outer diameter of the luer stubs and connectors compared to the inner diameter of the silicone tubing allowed for airtight press-fit connections to be made between the syringes and microfluidic device. As shown in Figure 3.9 the fluid was pumped from the syringes through the silicone tubing. Luer stubs were used to connect the syringe to the silicone tubing. Metal connectors were used to make the connection to the inlet ports of the PDMS microchannel by being directly inserted in to the punched holes in the PDMS discussed in the previous section. Similarly the exit consisted of a metal connector and a piece of silicon tubing that transported the liquid to an overflow container.

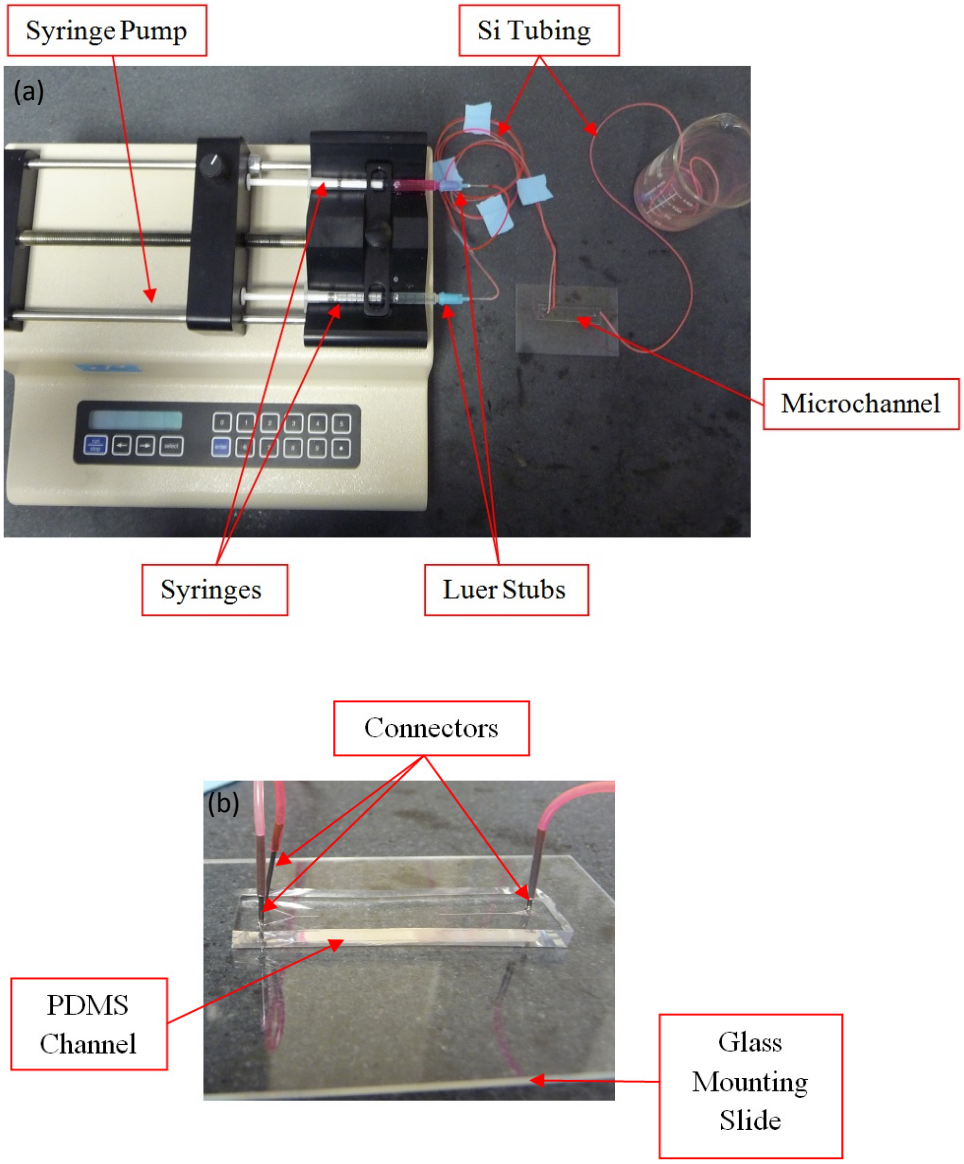

Figure 3.9: Experimental setup for the physical proof of concept study. (a) Fluid flow is driven by the pump through the syringes. The connection between the syringe and tube is made with a lure stub. Fluid is pumped through the inlets and outlet of the micromixer. (b) Connections between inlet and outlet tubes are made with hollow metal tubes. Connectors are inserted directly into the PDMS channel which is bonded to the glass mounting slide.

Achieving a stable microfluidic flow can often be challenging due to the large number of factors that can contribute to de-stabilizing a low volume flow. Any difference between the two inlet tube lengths or height would cause a difference in

hydrostatic pressure for each inlet, leading to non-uniform flow velocity. The limitations of the syringe pump used were also a factor in creating a stable flow, due to the pulsatile nature of the flow generated by the syringe pump at very low pumping speeds. The effect of this became more pronounced when two fluid streams were flowed together into the microfluidic device. In initial experiments, the flow often oscillated at the junction where the two flows met, as shown in Figure 3.10. The de-stabilized flow caused by the pressure difference varied from a constant pressure mismatch with a single dominating flow to an oscillating pressure difference switching the dominate flow from top to bottom.

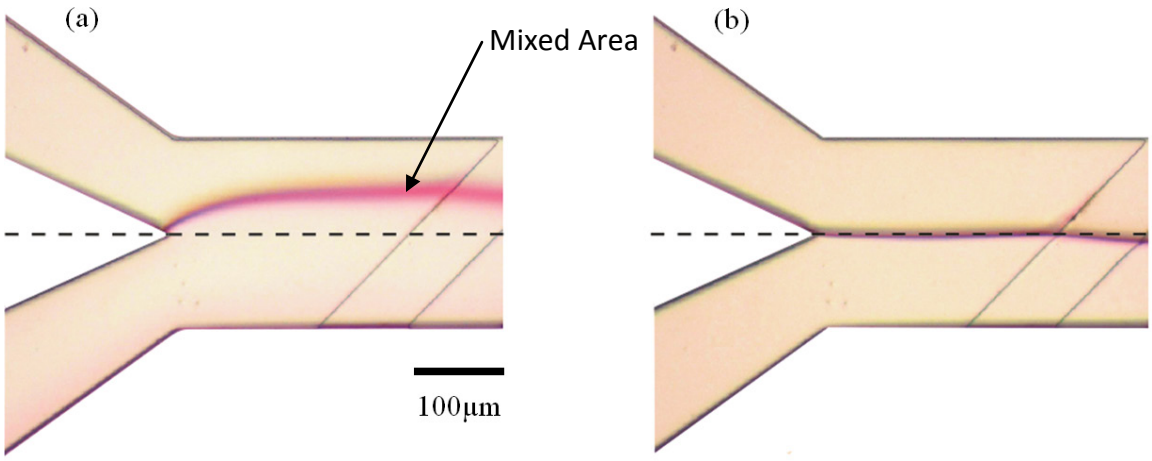

Figure 3.10: Fluid inlet junction: phenolphthalein solution (top) and sodium hydroxide solution (bottom); mixing of the two fluids produces a pink color at the interface. (a) Fluctuating fluid interface at Y-junction (b) stabilized normal inflow.

A design flaw in the layout of the inlet ports was found to be the largest contributor to the fluid oscillation. In the initial design shown in Figure 3.11(a), it was thought that an inlet reservoir much larger than the channel itself was needed to buffer any pulsing effects from the syringe pump. Since the mixer is molded with a flexible rubber, it was thought that any pulsing would be absorbed by the large volume and the

structural flexibility of the reservoir. However, due to the large size of the inlet reservoirs compared to the connector size, completely filling the reservoirs could not be accomplished reliably. The size of the air pockets formed in the reservoirs was not repeatable and caused the two fluids to meet at different velocities, creating an oscillating flow. In addition, the extreme decrease in size from the large reservoir to the inlet channel was thought to have had a possible throttling effect. Large fluctuations in pressure and velocity could occur due to the sudden throttle at the reservoir channel interface which could lead to an unstable flow.

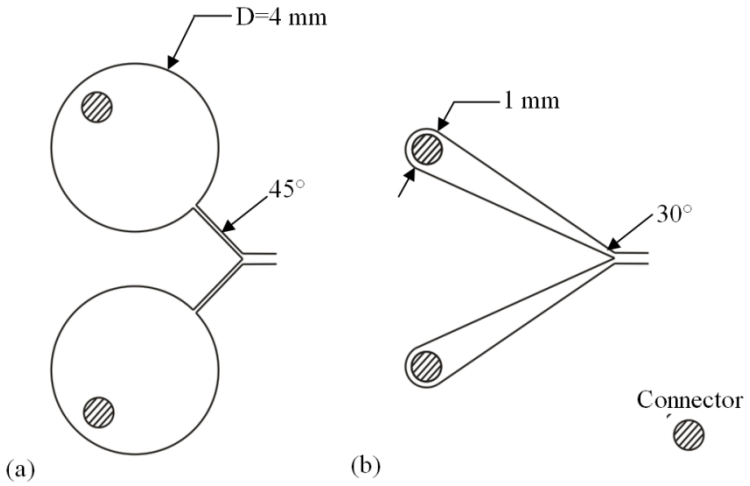

Figure 3.11: Inlet port designs: (a) initial inlet design with large reservoirs having a surface area of 12.56 mm^2 and (b) the revised inlet design with a decreased surface area of 3.53 mm^2.

Another area for concern was the angle at which the two fluids met; the initial design had an entrance angle of 45° for each inlet. Although T-shape micromixers with inlet angles of 90° have been used successfully in microfluidic devices, they were generally in applications that are insensitive to small fluctuations at the fluid junction [34]. In most micromixer studies concerning two inlet flows the junction often has a small entrance angle or sweeping curved entrance [5, 33]. By decreasing the inlet

entrance angle the velocity field for each flow will tend more toward the down channel direction rather than the cross channel direction when they meet. To facilitate this, the inlet angles of the revised design shown in Figure 3.11(b) were reduced to 30°. Also to eliminate the formation of air pockets the inlets were given a maximum tolerance of +.3mm over the connector to avoid trapping air pockets in the inlet space. This resulted in a 71.8% decrease in the area of the inlet footprint creating a much smaller volume reservoir to be filled. In addition, the inlets gradually reduce from the 1mm width to the .1mm width at the junction to reduce possible effects from a sudden throttling seen in the initial design.

3.3 Experimental Procedure

This section outlines the overall procedure used in setting up the physical proof of concept studies discussed in this chapter. First, volumetric flow calculations were made to determine the correct syringe pump settings to achieve the desired velocity in the channel of 3 cm/s. Volume flow rate of the syringe pump used in this study was set in units of µL or mL per unit time. To calculate the needed volumetric flow rate (Q), within the channel, the desired velocity (C) was multiplied by the smallest cross-sectional area of the channel (A):

$$Q = A \times C \tag{3-1}$$

For both featureless and SGM channels studied the smallest area A was a rectangular cross-section 70 µm by 200 µm. From here it was a simple conversion to a useable setting on the syringe pump:

$$Q = 0.00014cm^2 \times \frac{3cm}{s} = \frac{0.00042cm^3}{s} \times \frac{1{,}000\mu l}{cm^3} \times \frac{60s}{m} \qquad (3\text{-}2)$$
$$= 25.2\mu l/m$$

The volumetric flow rate Q was then divided by 2 since there are two syringes and inlet ports into the channel. Flow rate settings were experimentally confirmed by connecting the exit tubing to a small syringe and using the time taken to fill a given volume to calculate volumetric flow rate.

Once the settings for the syringe pump were calculated the microfluidic system was assembled. To start, two sections of silicon tubing of equal length were cut with enough length to reach from the syringe pump to the microscope being used for image analysis. A third piece of tubing was cut for the waste liquid coming from the channel exit. Metal connectors and luer stubs were then placed on either end of the tubing. Then two syringes were filled with each of the two fluids (A & B) to be pumped into the device, totaling 4 syringes. Any bubbles within the syringes are removed before proceeding any further. This is done by holding the syringe vertically and flicking the syringe forcing any air bubbles to the top of the syringe. The plunger is then depressed ejecting any air pockets in the syringe.

Four syringes were used in order to minimize the number of air pockets within the silicon tubing. The first syringe of fluid A was attached to the luer stub and the silicon inlet tube manually filled by depressing the plunger. Once the silicon tube was completely filled, the first syringe was disconnected and then the second syringe of fluid A was connected to the luer stub. This is done quickly to eliminate the formation of bubbles within the silicone tubing. The same procedure was then completed for fluid B. Once both silicone connecting tubes were filled, both syringes were placed into the

syringe pump. To ensure both syringes were in contact with the pushing block of the syringe pump and at the same volume, the pushing block was pulsed forward until fluid was seen coming from both metal connectors on the inlet tubing. Then the connectors for the inlets and the exit were inserted into the pre-punched holes in the microfluidic device. Finally the syringe pump was turned on at the appropriate pumping speed to flood the channel. The pump was allowed to run for 5-10 minutes to allow the flow to stabilize. Once the flow stabilized the channel was ready to be analyzed under the microscope.

Several factors such as air pockets within the tubing or height and length differences between the two inlet tubes could have an influence on the stability of the flow at the fluid junction. To avoid this, care was taken when cutting the tubes to be sure that they were of the same length, and both inlet tubes were taped together between the connections to the syringe pump and microfluidic device. This decreased any height difference between the inlet tubes which could have caused a difference in hydrostatic pressure from tube to tube. Whenever possible, the syringe pump and inlet tubes were placed above the microchannel to eliminate pumping against gravity. Likewise the exit tube ran to a waste container that was placed below the microchannel.

3.4 Physical Fluid Behavior Study: Results

The slanted groove micromixer geometry used in this research uses diffusion and chaotic advection to mix the inlet fluids together. As discussed previously, the mixing is achieved by creating a fluid flow that will increase the contact surface area between the two fluids allowing for more area of diffusion. Specifically, the slanted groove

micromixer works by creating a rotational flow that folds the two fluids over one another, creating the increased contact surface area needed for faster diffusion.

Because glass was used as the bottom surface of the micromixer, it was possible to image the system using traditional inverted or confocal microscopy. For the physical studies in this chapter, all channel dimensions were as follows; h=70 μm, w=200 μm and when grooves are present h'=9 μm, w'=100 μm and θ=45° (dimensions from Figure 2.3). The process used to make the mold made it challenging to exactly match the 7 μm feature height used in simulations, but since the feature height was much smaller in comparison to the channel height the 2 μm difference in feature height was assumed to be acceptable.

Several techniques were used to visualize the diffusion interface in the SGM and featureless channel. The first method used a pH indicator (phenolphthalein) which is translucent in the presence of an acidic solution but turns pink in the presence of a base solution. The solvent used in both inlet fluids was ethanol with one fluid 2% phenolphthalein and the other 2% sodium-hydroxide. This caused the diffusion interface between the two liquids to turn pink while unmixed fluid of either type remained translucent. It should be noted that in the images below, the presence a pink hue does not necessarily indicate areas of complete mixing only areas where mixing has begun; areas without a pink hue are completely unmixed. The concentrations of each fluid at each area showing a pink hue cannot be calculated. Figure 3-12 illustrates the diffusion of the two fluids across the featureless channel through this visualization technique.

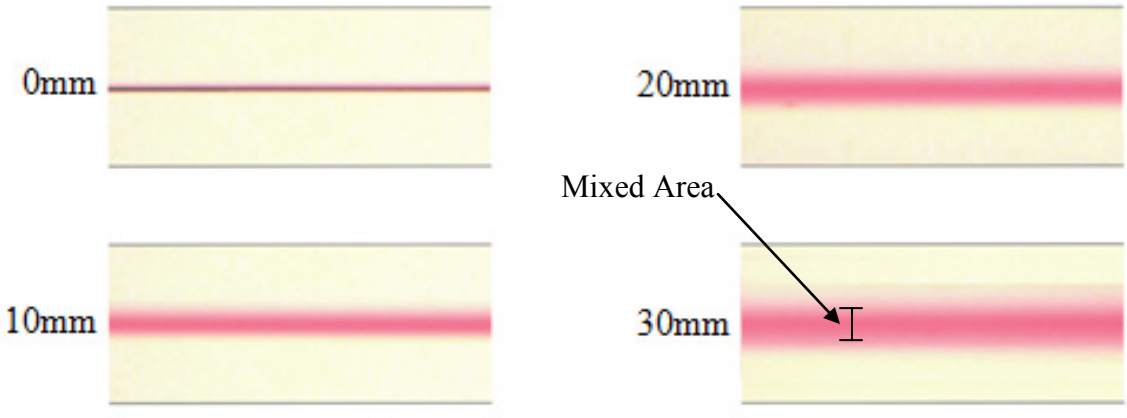

Figure 3.12: Optical micrographs of a featureless channel with Phenolphthalein tracer dye (top) and NaOH solution (bottom). Top down view taken every 10 mm from the inlet. Channel width is 200 µm.

As expected, no chaotic flow is present in the featureless channel; this is verified by the single, straight line in the center of the channel where diffusion has occurred. The small interface between the fluids greatly increases the length required to fully mix. With such a large distance required to fully mix any advantages gain by miniaturizing the channel are lost. After 30 mm of travel the farthest the interface of either liquid has diffused across the channel is 25-30 µm away from the centerline of the channel. This leaves up to 75% of the volume of the channel completely unmixed with the remaining volume at different stages of mixing. This outcome agrees with the computational models presented in Chapter 2 displaying a laminar non-chaotic flow throughout the length of the channel.

The difference in mixing efficiency caused by grooved features was assessed by performing the same analysis on a channel with the addition of slanted grooves. All grooves were created with a width of 100 µm, height of 7 µm and repeated at an interval of 100 µm. All features had sharp edges due to the limitations of the photolithography

process, unlike the simulations run in Chapter 2. However, the results were expected to be qualitatively similar. Figure 3-13 shows the results obtained using a SGM channel with the same Phenolphthalein/NaOH visualization technique as in the featureless channel.

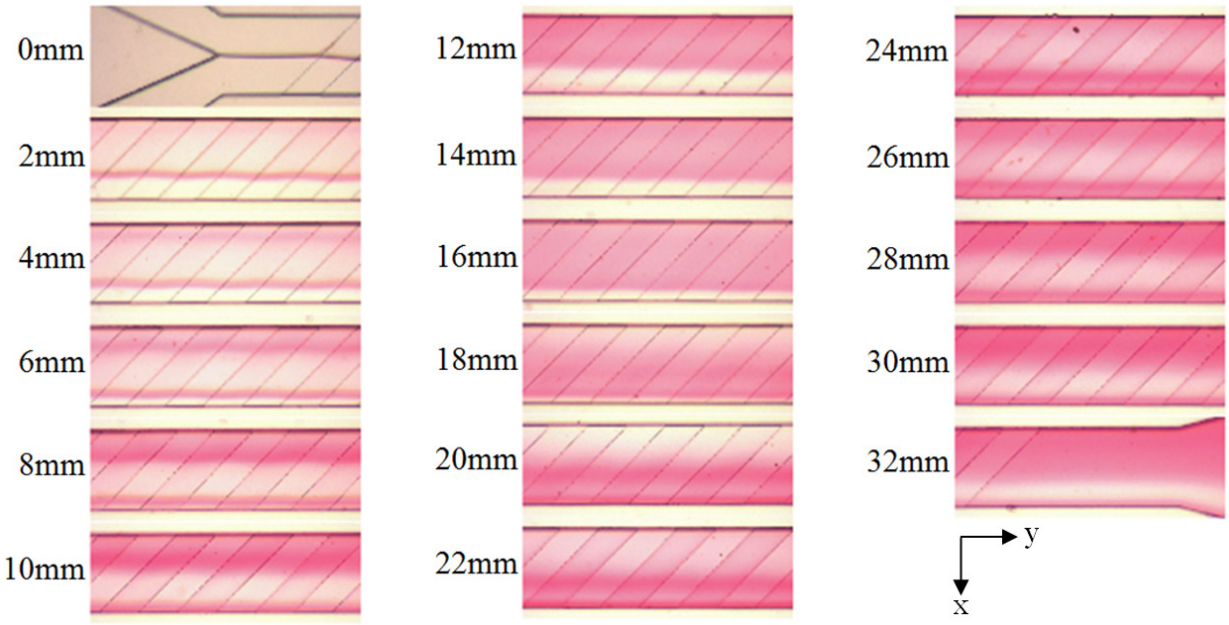

Figure 3.13: Optical micrographs of a SGM mixer with Phenolphthalein tracer dye (top) and NaOH solution(bottom). Top down view taken every 2 mm from the inlet. Channel width is 200 µm.

In Figure 3-13, the initial fluid interface can be seen in the 0mm image with only the initial diffusion interface visible. As the fluid traveled in the +y direction, the interface line moved across the channel in the +x direction away from the centerline as opposed to the stable interface in the featureless channel. As the initial interface line moved to the lower channel wall, the area of diffusion indicated in pink also began to appear along the upper channel wall due to the rotation of the diffusion interface within the channel. Although a rotational flow is evident in Figure 3-13, the quality of mixing and expansion of the diffusion interface could not be assessed in detail. Despite this, the

SGM showed a large increase in mixing efficiency over the featureless channel. By following the fluid interface throughout the images, it can be concluded that the flow completes 1.5 to 2 rotations. For a more detailed analysis of the rotating fluid interface, different visualization methods were necessary.

In order to gain an understanding of how the fluid flow was reacting to the slanted grooves in the physical model, it was necessary to view both the x-y plane and x-z plane using confocal microscopy. Cross-section views allowed for the analysis of rotation for the slanted grooves as well as comparison to computational findings from Chapter 2. To visualize the flow accurately, fluorescent dye (fluorescein) was used instead of phenolphthalein. Fluorescein dye fluoresces in the 494 to 521 nm wavelength range and appears green when excited. Water was used as the base fluid for both inlets since fluorescein is water soluble with one inlet of pure de-ionized water and the other mixed with fluorescein.

For imaging purposes of this study, a Leica TSP SP5 Inverted Confocal microscope with x, y, and z scanning capabilities was used. The three axis scanning capabilities allowed for fluorescent scanning in any plane, which allowed for the capture of cross-section images of the SGM and featureless channels. For excitation of the fluorescent mixture, an argon and helium-neon laser was used. All confocal microscopy images were obtained in the Imaging Facility operated by Mary Engle and Jim Begley in the Biomedical Biological Sciences Research Building at the University of Kentucky.

Confocal images of the cross-sectional mixing profile were obtained for both a featureless channel and SGM channel. First the featureless channel was tested to allow

for a baseline of comparison for the SGM. The featureless channel will show the diffusion present just at the vertical interface between the two fluids. Cross-sectional images of the featureless channels were taken every 2 mm from the inlet; the images are shown in Figure 3-14 with the fluorescein solution appearing in green and the DI-water shown in black.

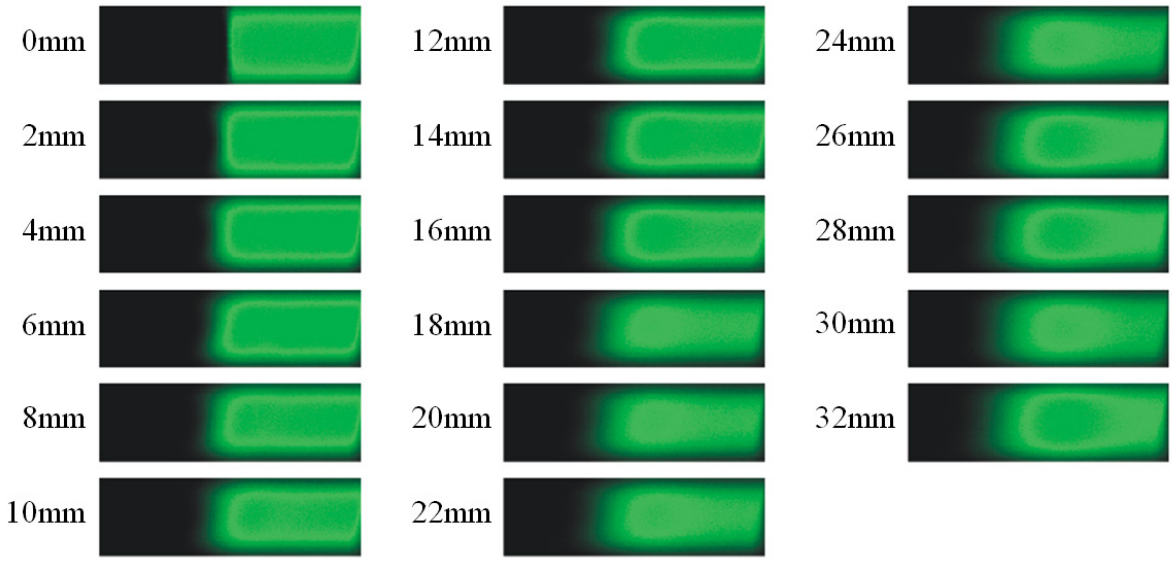

Figure 3.14: Confocal microscopy images of the featureless microfluidic channel: cross-section views showing diffusion interface taken every 2 mm. Channel cross-sectional dimensions are 200 by 70 µm.

As expected the only area in which mixing occurs is at the interface between the two fluids. Comparing the images at 0 and 32 mm shows the total diffusive travel of the fluorescein to be approximately 50 µm past the centerline. This is an increase in diffusive travel as compared with the phenolphthalein study shown in Figure 3-12. But due to the limitations of the microscopy equipment, some background noise is present around the fluorescein solution.

Another factor that could contribute to an increase in diffusive travel is the phenomenon known as the butterfly effect. This is the tendency for fluids to diffuse further at the top and bottom of the channel since the molecules have a longer residence time in these regions of the channel [37]. The longer residence time is due to velocity profile of the channel with the greatest velocity occurring at the center of the channel and decreasing in the direction of the boundaries. Figure 3-14 depicts the curvature of the fluid diffusion interface due to the butterfly effect. Because of this and the noise produced by the microscope, it was difficult to determine the exact diffusion line

Figure 3.15: Confocal microscopy images of featureless channel cross-section at 2mm from inlet. Dashed line shows approximate diffusion boundary between the two fluids, demonstrating the "butterfly effect."

A SGM channel was observed in a similar manner using confocal microscopy; the resulting cross-sectional images display rotational flow, shown in Figure 3-15. Due to limitations of the imaging equipment, the images show only the main body of the fluorescein solution. Once the fluorescein solution diffused into the DI-water solution, the fluorescent signal became weaker and no longer appeared in the images. For this reason it was difficult to obtain a quantitative measurement of the percentage mixed from these images. But by following the main body of the fluorescent stream, the rotational effect of the SGM could be quantified. A significant rotational effect was apparent , with

the fluorescent stream being swept over the slanted grooves. The resulting flow rotated in a clockwise motion following the positive direction of the slanted grooves as illustrated in Figure 3-16.

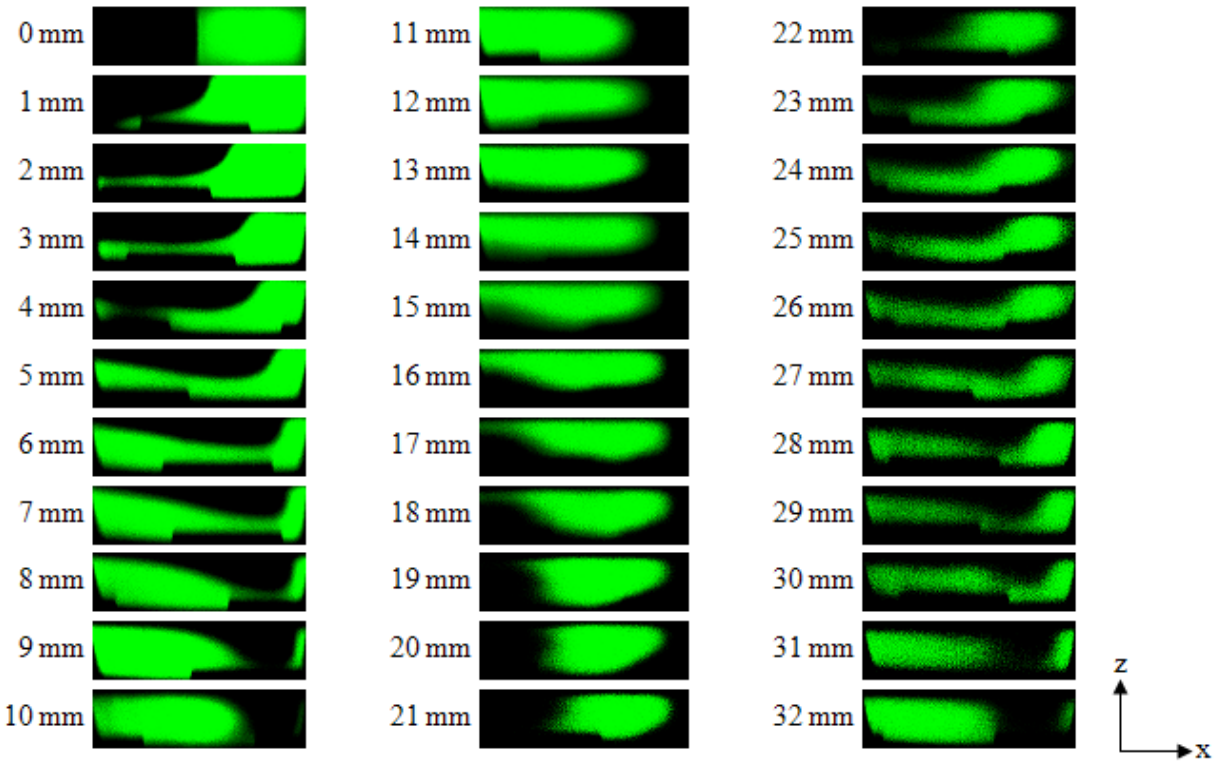

Figure 3.16: Confocal microscopy images of SGM: cross-section views showing diffusion interface and fluid rotation taken every 2 mm. Channel cross-sectional dimensions are 200 by 70 µm.

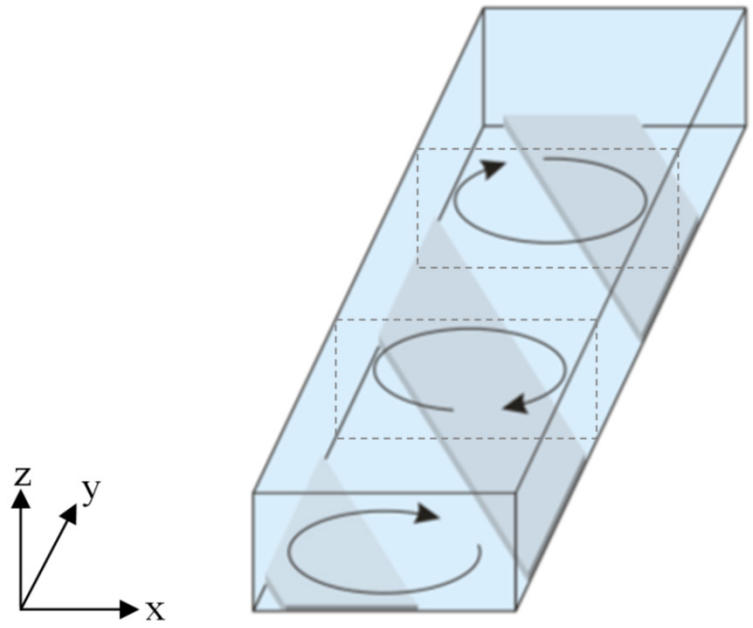

Figure 3.17: Clockwise rotation in SGM as fluid flow moves in the positive y-direction. Coordinate system corresponds to that in Figure 3-15.

Since the only contributing factor to rotational flow is the slanted grooves, the direction of the rotation is controlled by the angle of the grooves. As shown in Figure 3-16, the fluid at the bottom of the channel moves from right to left in the positive y-direction at the surface containing the slanted features since the features also move in this direction. This corresponds to the direction of the flow observed in experiments shown in Figure 3-15. The images in Figure 3-15 also show the relative speed of rotation with the main body of fluorescein switching sides (180° of rotation) every 10-11 mm, completing a total of 540° of rotation by the 32.33 mm distance.

The mixing efficiency is not only increased by the lengthening of the single diffusion interface barrier present at the inlet, but also by creating multiple new interfaces between the two liquids. This is done by separating smaller sections of one fluid into the other or folding the fluids into one another. This phenomenon is demonstrated in the

9 mm and 31 mm images in Figure 3-15. Unfortunately, the multiple segments of fluid created in this model cannot be imaged accurately due to the resolution of the microscope. This is due to the microscope only being able to pick up the highly concentrated areas of fluorescence. Once a section of fluorescent liquid folds into the non-fluorescent solution, the diluted fluorescent signal becomes difficult to capture. Despite the limitations of the imaging equipment, a strong rotational flow and its folding effect can be observed with these images.

3.5 Conclusions

A significant mixing effect was accomplished in the PDMS micromixer experiments in this research. Both visualization methods (phenolphelein and flouerscein tracer dyes) showed minimal diffusion when flowing in a featureless channel. This lack of diffusion represents a completely laminar flow with advection occurring primarily in the direction of the flow. In contrast, the SGM channels showed a significant increase in mixing over the featureless channels. Both methods showed 1.5-2 complete rotations of the two fluids within the channel. This rotational flow caused by the SGM features increases the chaotic advection across the channel which increases the surface area for diffusion between the two liquids. Overall the low profile features modeled in this experiment caused a rotational flow to develop resulting in chaotic advection across the channel.

Chapter 4: Shape Memory Alloy Micromixer

To obtain a controllable chaotic micromixer, a Ti-Ni shape memory alloy plate was combined with a PDMS microchannel to form a complete system. By making the micromixer grooves from a shape memory alloy, the features within the channel can either be turned on (protruding) or off (flat) by changing the system temperature. The ability of stationary microgrooves to affect the mixing of such a flow has already been demonstrated in Chapter 3, but this chapter focuses on the fabrication and integration of a complete SMA micromixing system.

4.1 Ti-Ni Microscale Surface Feature Fabrication

In order to create a SMA micromixer, it was necessary to generate controllable features on a SMA surface. The method chosen for creating these reversible microstructures was two-dimensional plane indentation. . The indentation method uses Hertzian contact along with the load-displacement relationship between a rigid indenter and an elastic plane to generate microscale features in a surface [27]. In order to create a series of patterned grooves for these experiments similar to those used in the computational and proof-of-concept models, small diameter (76.2 μm) tungesten rods were depressed into the surface of the Ti-Ni alloy [19]. Once the indents are made, a series of polishing and heating steps were performed to make reversible 2.way microfeatures. The details of this process are included in the following sections.

4.1.1 Ti-Ni Surface Preparation

Due to the very small diameter of the tungsten wire to be indented (76.2 μm), it is necessary to have a smooth SMA surface prior to indentation. This ensured that a change

in the surface of the SMA material was caused by the uniformly distributed force of the wire against the material and not in nonuniform, discrete locations caused by pre-existing scratches or imperfections in the material. To do this the surfaces are first ground using multiple steps with increasingly smaller grits: 400 grit (18.3 µm), 600 grit (10.6 µm) and ending with 1200 grit (3.8 µm). For all steps in the grinding and polishing process SiC (silicon carbide) is used as the abrasive or grit [28]. During each step water was continually flowed onto the grinding pad to lubricate the sample and paper, easing the process by decreasing the overall friction. The grinding direction of the sample was changed by 90° after each change in grit which allowed for visual determination of when all scratches from the previous larger grit were removed; this is illustrated in Figure 4.1.

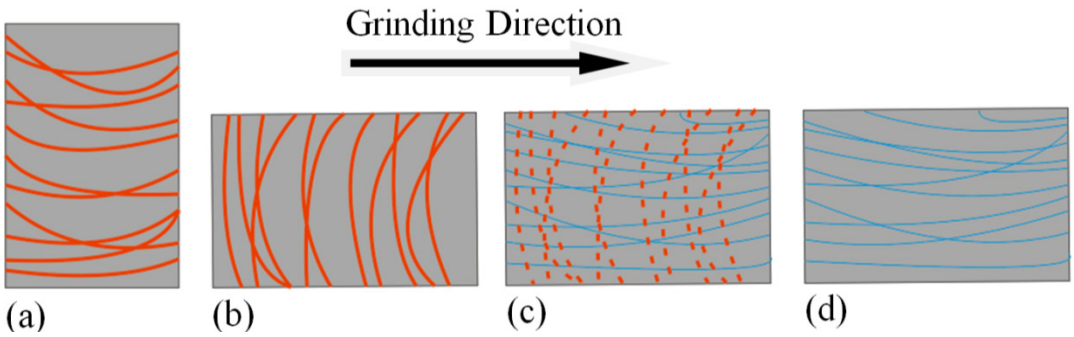

Figure 4.1: Grind procedure for Ti-Ni (direction of abrasion is from left to right): (a) Sample is ground using grit X until the only abrasion marks seen are horizontal. (b) Sample is turned 90° so abrasions from grit X are now vertical. (c) Sample is ground using finer grit Y, abrasions from grit X are removed as abrasions from grit Y appear. (d) Sample is ground until only horizontal abrasions from grit Y are left. This protocol is repeated each time the grit size is changed until sample is fully polished.

After the surface was uniformly ground to an average surface roughness of 3.8µm using the 1200 grit paper, the sample was further polished using a SiC paste slurry incrementally decreasing the grit size of the paste down to 50 nm. The details of the

grinding and polishing steps are listed in Table 4.1. These processing steps results in the smooth, mirror like surface finish seen in Figure 4.2.

Table 4.1: Protocol for grinding and polishing of SMA samples.

Polishing Steps and Procedures	
Grinding	A grinding wheel with interchangeable grit papers was used for initial grinding. Water is continually flowed onto the paper to reduce friction and cool the samples.
400 Grit Paper	Place the 400 grit paper on the wheel securing it to the wheel with the metal ring. Note: if a sample has a high surface Ra it may be necessary to start with larger grit (320 or 240).
Water Control	Turn on the water source. Turn on water arm and position the flow so it is hitting the center of the paper to ensure full coverage of the water. Turn on bowl wash.
Speed Control	Turn on grinding wheel to desired RPM setting.
Sample Grinding	Firmly hold the sample with both hands. Make sure your hands and gloves are clear of the surface to be ground. Apply pressure with the sample to the grinding pad. Take care to apply even pressure so wear is evenly distributed on the surface (this is more difficult with samples that have large surface areas). Approximately 10 min. for each grit paper.
Change Paper	Once the sample is sufficiently ground to the current grit size change the paper to a finer grit. Repeat the above steps for the new grit size while positioning the sample as illustrated in Figure 4.1.
Grit Progression	Use the above procedures starting with the largest grit and sequentially using smaller grits until the 1200 grit paper is used. Normal progression consists of 400, 600 and 1200 grit papers with 240 and 320 grits added at the beginning if needed.
Polishing	A polishing wheel with interchangeable polishing pads was used/
Water Control	Turn on the water source. Turn on water arm and bowl wash. Rinse grinding pad but do not position the arm to flow on the pad during the polishing steps.
Speed Control	Turn on polishing wheel to desired RPM.
Sample Polishing	Shake the bottle containing the 3µm slurry bottle and dispense a small amount of the solution onto the center of the pad. Apply pressure with the sample to the polishing pad. Re-apply slurry when needed until done. Approximately 15 min. for each slurry size.
Change Slurry	Once the sample is sufficiently polished to the current grit size of the slurry rinse the polishing pad of all grit. Repeat the above polishing steps with using finer grit slurry using the same positioning steps illustrated in Figure 4.1.
Grit Progression	Use the above procedures starting with the largest grit slurry sequentially using smaller grit slurries until the 50 nm grit slurry is used. Normal progression consists of 3 µm, 1 µm, 500 nm and 50 nm. Note: 3 µm and 1 µm slurries use a different pad than the 500 nm and 50 nm slurries.
Final Polishing	Once the finest grit slurry has been used finish by flowing only water onto the pad. Polish until desired finish is reached.

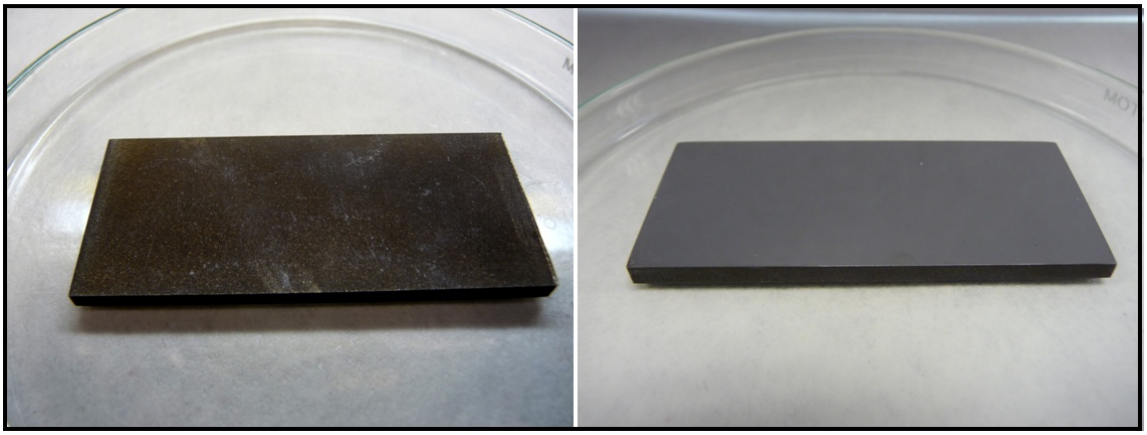

Figure 4.2: Surface of Ti-Ni SMA before (left) and after (right) grinding and polishing procedures.

The resulting average surface roughness of the Ti-Ni surface was measured using a Zygo New view interferometer and found to be 0.396 μm and 0.056 μm R_a after grinding and polishing, respectively. The final polishing value was considered to be low enough that any subsequent indentations made in the Ti-Ni surface would be attributable to the indenting process and not pre-existing surface roughness. After polishing was complete the next step was to physically make the indented features on the polished surface.

4.1.2 Material Properties

Three different components were needed for the micro indentation process: the polished SMA, a small diameter metal rod, and a highly rigid stamp. The components needed to be arranged in series in an indentation machine, as shown in Figure 4.3. For the metal rods to be efficiently indented it is important to use a metal that is harder and stronger than the Ti-Ni alloy to minimize deformation of the rods. As in previous work using this method [19], tungsten rods were chosen because of its high bulk modulus and

hardness. Lastly the stamp/punch that was used to drive the rod into the SMA surface was made of S7 tool steel. It was important to ensure that the punch used to press the rods into the SMA was harder than the SMA surface allowing for it to be considered rigid. If it was not significantly harder than the SMA material, indentations could also form on the surface of the punch.

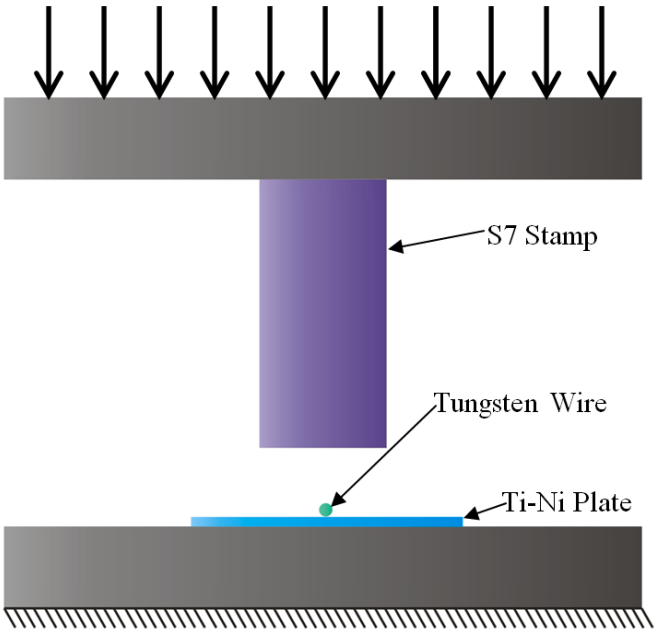

Figure 4.3: Schematic of S7 steel punch pressing tungsten wire in Ti-Ni plate (not to scale).

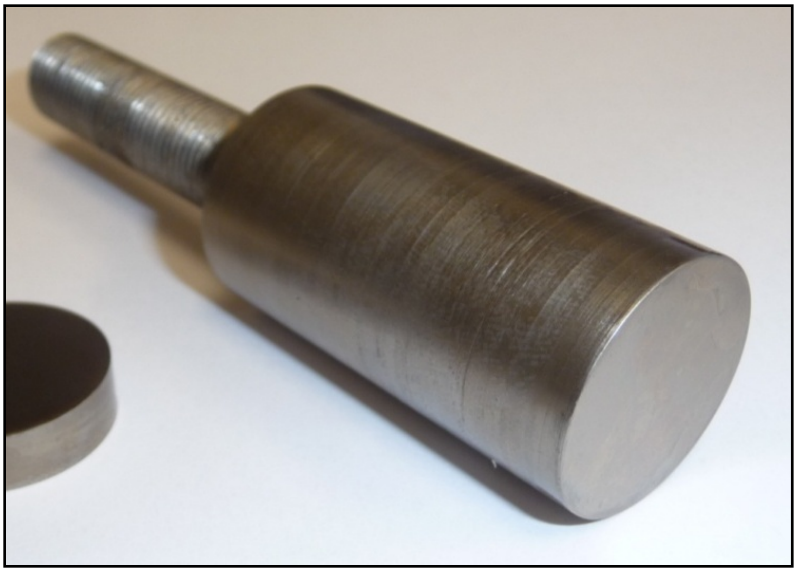

Figure 4.4: S7 tool steel machined component: threaded punch 1" diameter.

The S7 steel punch (Figure 4.4) was machined in the University of Kentucky machine shop. This specific steel was chosen because of its high impact resistance and ability to be hardened through heat treatment. The material composition of the S7 tool steel consisted of 0.45-0.55% C, 0.20-1.00% Si, 1.30-1.80% Mo, 0.20-0.80% Mn, 3.00-3.50% Cr, and the remaining balance iron [29]. The hardening process involved heating the parts to 1250°F and allowing them to thoroughly soak to relieve any internal stresses. Then the temperature was raised to 1725 to 1750°F and the parts were soaked for 45 to 60 minutes per inch of thickness.

Material hardness was tested for the Ti-Ni alloy and the for the S7 steel component before and after heat treatment using a mechanical indenter. The results of these tests demonstrate why the heat treatment process was necessary; without this extra processing step, the steel punch would have been substantially softer than the Ti-Ni alloy and would have absorbed most of the deformation during the indentation process. The

hardness of the treated S7 is also in good agreement with typical hardness values for the prescribed heat treatment process, which usually ranges from 58 to 60 C on the Rockwell scale.

Table 4.2: Hardness measurements on the Rockwell C hardness scale using diamond tip indenter for Ti-Ni and S7 tool steel.

Material Hardness Chart Rockwell C (HRC)						
Metal	**Indent 1**	**Indent 2**	**Indent 3**	**Indent 4**	**Indent 5**	**Average**
Ti-Ni	20.5	22.0	21.5	21.0	21.0	**21.2**
S7	10.8	11.0	10.6	10.2	11.0	**10.7**
S7 Heat treated	59.5	59.0	58.5	59.0	59.0	**59.0**

Although the tungsten wires were too small to perform any hardness tests, it is known that tungsten is a very hard metal with an average hardness ranging from 6.0 to 7.5 on the mohs scale [30], compared to an average of 5.5 on the mohs scale for heat treated S7 steel. Tungsten also has a high resistance to compression with a bulk modulus of 310 GPa in its raw form [30]. Since it was already known that a tungsten rod can produce good indentations in a Ti-Ni surface [19], it was sufficient to show the increased hardness of the S7 steel punch over the Ti-Ni plate.

4.1.3 Indenting Procedure

To indent the surface of the SMA an Instron material tester was used to apply a uniform compressive force to a 76.2μm diameter 2mm long Tungsten rod. To perform the indentations, the Ti-Ni plate was placed onto the center of the load cell platform. Once the piece is centered, a tungsten wire was placed onto the Ti-Ni surface in the desired location for indenting. When creating multiple patterned indentations, the wires were placed onto the surface of the metal before compression and held in place by a small

amount of wax to ensure minimal movement of the wires from their desired location. Once the wires were in place, the top punch attached to the upper arm of the Instron was lowered into place directly above the wire but not in contact. Once the punch was in place, the loading program was started. All loading programs were set to advance at a rate of 0.05mm/min until the desired compressive loading was reached. Once the desired loading was reached, the program stopped and the sample was held at that loading for one minute after which the upper arm was moved up, releasing the load.

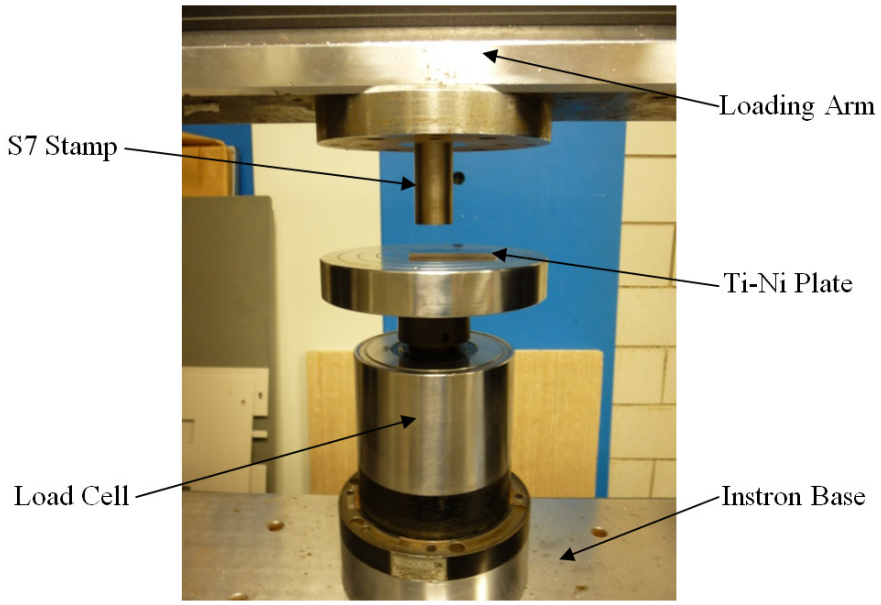

Figure 4.5: Instron compression machine being prepared to stamp tungsten wire into Ti-Ni plate via S7 steel punch.

Figure 4.5 shows the complete compression machine assembly. The S7 steel punch was attached to the dynamic upper loading arm, which was lowered down to drive the tungsten rod into the Ti-Ni plate that was resting on the base/load cell. The indentation process was initially performed with a single Tungsten rod at multiple loads to determine a relation between indentation depths and loading; Figure 4.6 illustrates this relationship.

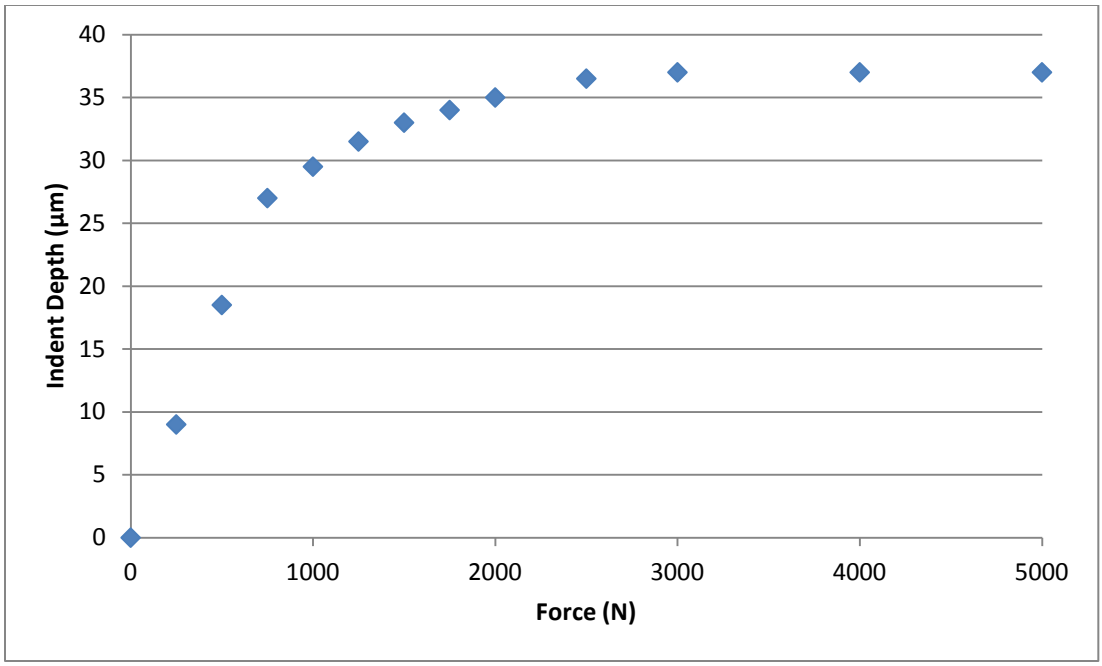

Figure4.6: Indentation force to depth relationship for tungsten wires of diameter 76.2µm and 2mm in length on a polished Ti-Ni surface.

Figure 4.6 shows that indentation depth increased with force up to the 2,500-3,000N range, where the indent reaches a maximum depth of 37 µm. Although the diameter of the wire is 76.2 µm the maximum achievable depth is only 37 µm due to the deformation of the tungsten wire. Although multiple indents at each indenting force were not taken indentation depth was found to be repeatable at 2,000N and above. To achieve repeatable depths at various forces the length of the wires should be controlled. In this study the tungsten rods were maintained at 2mm in length. Figure 4.7 shows the 3-D profile of the maximum indentation of 37 µm taken with a white light profilometer.

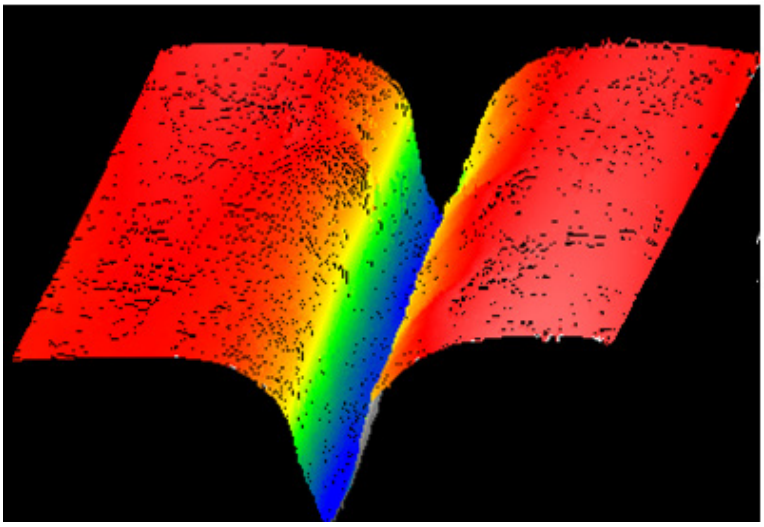

Figure 4.7: Micro-indent in Ti-Ni surface with an average depth of 37 µm formed from 76.2 µm Tungsten wire at 3,000 N.

Because the maximum possible depth of indentation was desired, all samples fabricated for use in the mixing system were indented with a force of 3,000 N. Any further force would have been unnecessary and could have lead to further deformation of the wire that could have a negatively affected the width of the resulting indents.

After the indentations were made, the SMA surface had to be processed to obtain two-way reversible features. This was done by following the procedure described in Chapter 1. First the sample was heated to its Austensite phase which caused partial recovery of the indentation; in this case, the sample was held at 423K for 5 minutes. After heating the sample, it was cooled to its martensite phase at 193K for 5 minutes. Then the system was allowed to return to room temperature. The indent once cooled back down will never be as deep as the initial indent. The cooling and heating temperatures are well above and below the respective phase transformation temperatures (table 4.3) for Austenite and Martensite to ensure the sample reaches each phase of the cycle.

Table 4.3: Phase transformation temperatures of bulk Ni-Ti alloys [19].

	T (Kelvin)	T (Celsius)
Austenite Start A_s	350	77.85
Austenite Finish A_f	404	131.85
Martensite Start M_s	344	71.85
Martensite Finish M_f	287	14.85

The surface profiles were measured during each step of this procedure, and are shown in Figure 4.8. This technique gives three distinct profiles of the indentation: initial martensite indent, heated austenite indent, and the cooled or recovered martensite indent .

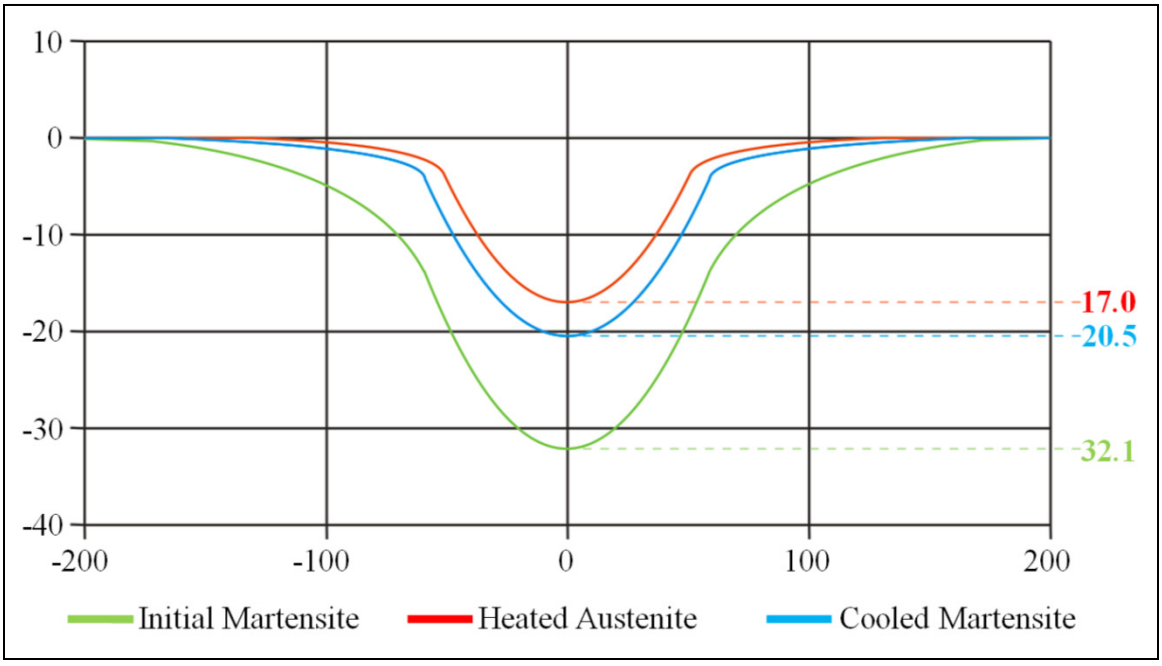

Figure 4.8: Titanium-Nickel indentation profile: height (y-axis µm) vs. width (x-axis µm) from 76.2µm Tungsten wire under 1,500N load.

Figure 4.8 shows the significant one-way recovery from the initial martensite phase to the cooled martensite phase after heating with a height difference of 11.6 µm. In addition the difference in profile height and width from the heated austenite to cooled

martensite phases illustrates the desired reversible characteristic of the material. To show the recovery of the Ti-Ni at various indent loadings profiles were taken of each indent at all three heating phases; the results are shown in Figure 4.9 below.

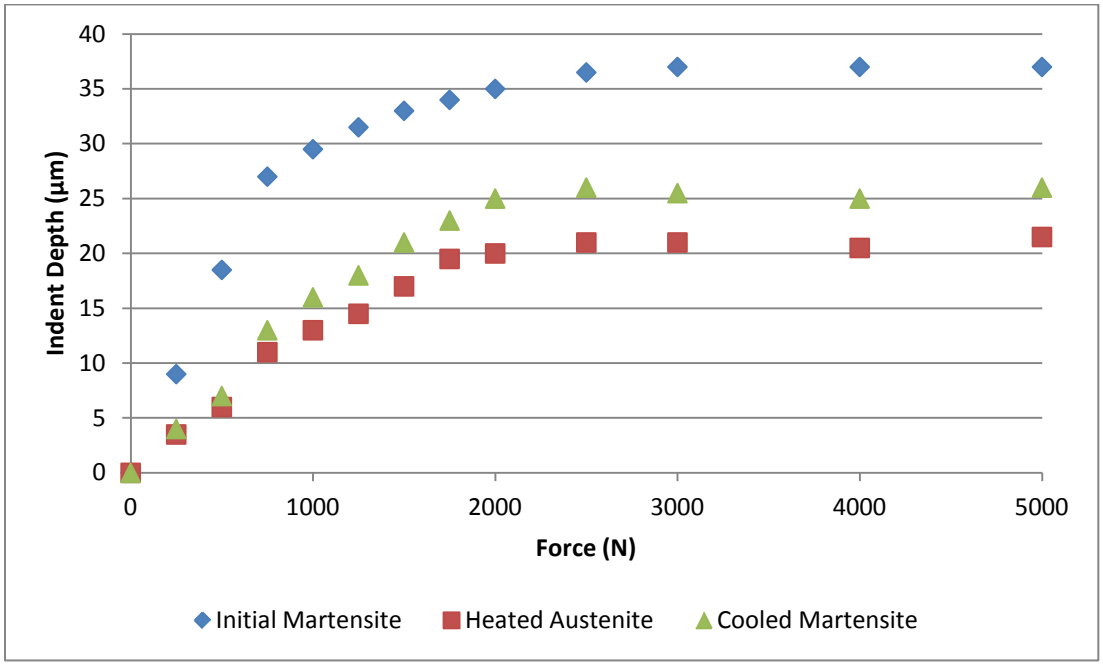

Figure 4.9: Indent depth at various loadings and heating stages.

Figure 4.9 shows that the indent depth had a direct affect on the resulting reversible height between the heated austenite and cooled martensite phases. The reversible cyclic depth increased with increase indent depth/force.

Although the indents were partially recovered at this stage, there were still areas of internal stress within the material that allow for the shape change between the Martensite and Austensite phase [20]. At this state, the indents would show a depth change when heated and cooled but would still be present in both phases. To obtain reversible features between a flat and featured surface the indents had to be polished flat. The amount of material removed in this process was equivalent to the depth of the

indents in when the material was in the Martensite phase. Once the planarization step was completed there were still areas of internal stress that when heated would produce a protrusion and return to the flat surface when cooled. This concept is illustrated in Figure 4.10.

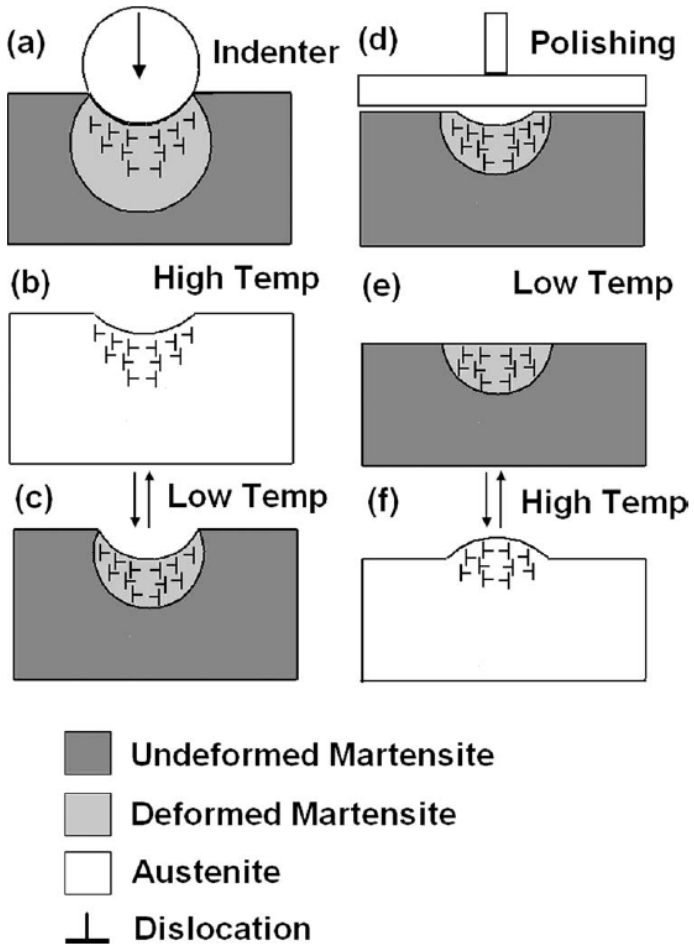

Figure 4.10: Experimental procedure for micro-indenting process. (a) Indenter deforms surface in Martensite phase. (b) Partially recovery when heated to Austensite phase. (c) Cooled back to Martensite with deeper indent than Austensite phase. (d) Polishing off indent in Martensite phase. (e) Flat surface with residual areas of internal stress. (f) Raised bump in area of internal stress in Austensite phase. Figure taken from [19].

Image (e) in Figure 4.10 shows the internal stresses that remained from the martensite indenting stress. This residual stress distribution is what allows for the

formation of the micro-structures when heated. The features are a result of the material moving to release the internal stress in its heated state. Figure 4.11 shows a surface profile of one of the reversible protrusions that was obtained from the indentation method discussed above.

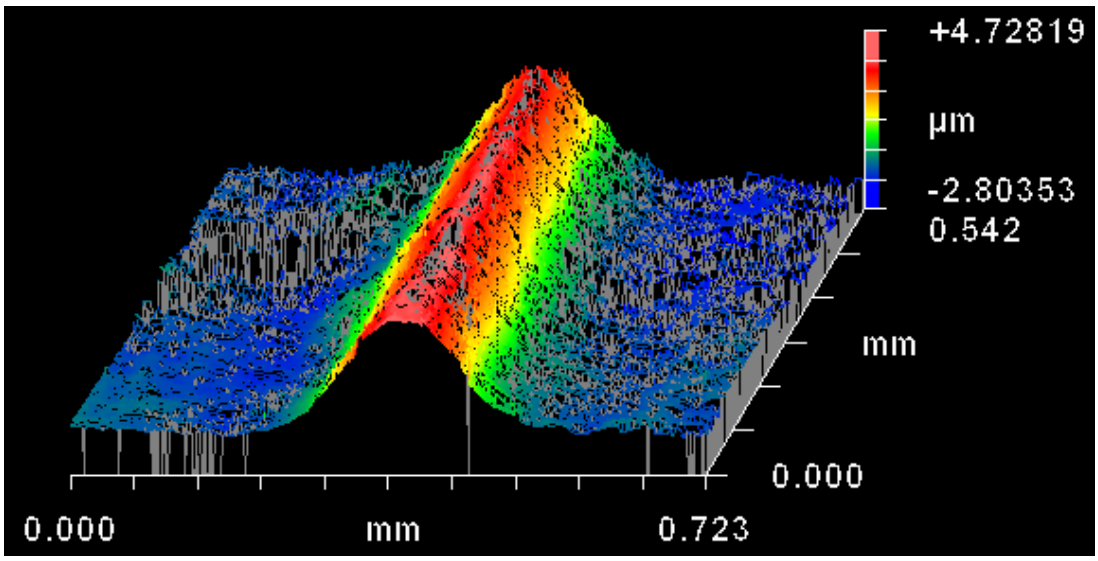

Figure 4.11: Protruding feature when Ti-Ni was heated to 160 °C. Average height of 7 µm.

The resulting reversible feature was obtained from a planarized 37 µm deep indent made by a 76.2 µm diameter wire. The height of the feature was found to be ~7 µm by averaging 15 separate profiles of the feature. On the subsequent cooling of the Ti-Ni plate, the feature returned to its planarized state, demonstrating the successful creation of a reversible micro structure controllable through the application of heat.

4.2 Ti-Ni Mixer Fabrication

In order to create a functional SMA micromixer, a rectangular microchannel molded in PDMS was placed on top of the Ti-Ni plate and aligned with the micro features. Since PDMS is an elastic rubber, when the microfeatures were activated the

PDMS would flex and allow the grooves to form within the microchannel. In order to actuate the microfeatures created on the Ti-Ni surface, a thermal-electric heater was incorporated into the system.

In order to obtain a steady microfluidic flow within the channel, a good seal had to be made between the PDMS channel and the substrate it is mounted on. Previous adhesion methods used for the proof of concept physical mixer discussed in Chapter 3 were not applicable for the Ti-Ni mixer fabrication since there are no adhesive properties created between PDMS and metals through plasma treatment.

Multiple methods were attempted to achieve a suitable adhesion between the PDMS channel and the Ti-Ni surface for a steady microfluidic flow. First an adhesion promotion chemical formulated to increase adhesion between PDMS and metals was used. The chemical was applied in a thin coat to the surface of the Ti-Ni plate, and the PDMS microchannel was placed on top of the plate and the chemical was allowed to dry. Once dried, a negligible increase in adhesion was observed, but the seal failed once any fluid was flowed through the channel, resulting in a complete loss of adhesion.

Next, to take advantage of the strong bond that can be formed with PDMS through plasma treatment, a thin coating of PDMS was spun coated onto the surface of the Ti-Ni plate. Since PDMS is a flexible rubber, the microfeatures on the Ti-Ni surface will transmit their profile through the PDMS layer. Due to the micro scale of the features, a very thin layer of PDMS (500 nm-1,000 nm) was required to allow the features to transmit their shape through the PDMS effectively. Since liquid PDMS is very viscous when uncured, it was necessary to thin out the PDMS with a thinning agent.

When using a sufficient thinning agent, PDMS can be spin coated down to a thicknesses below 100 nm [31]. In initial experiments for obtainable thickness, toluene was used to thin the PDMS and was spun on a glass substrate with the resulting thickness vs. mixing ratio shown in Figure 4.12.

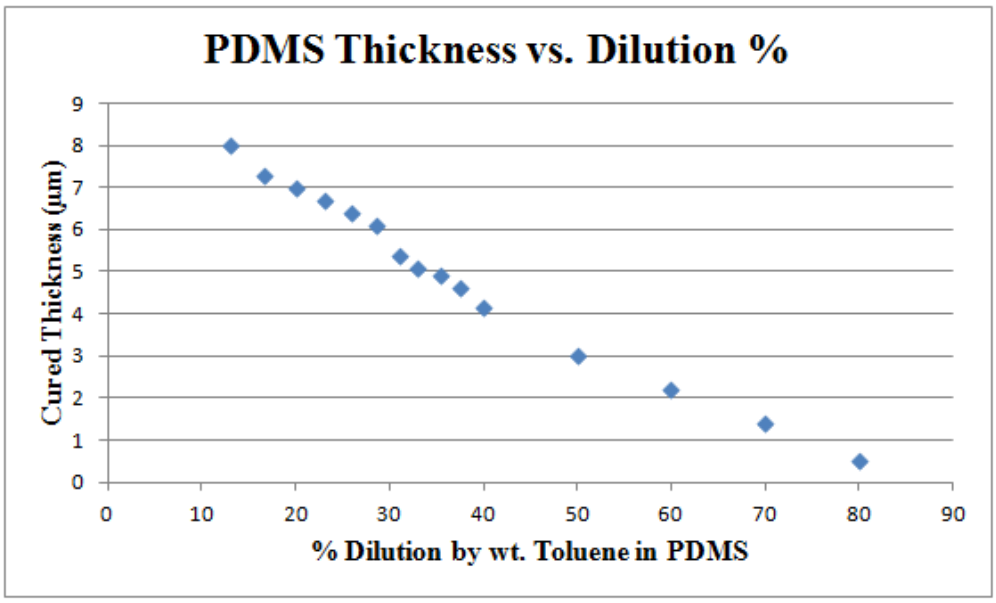

Figure 4.12: Cured thickness of PDMS vs. dilution percentage when spun coated on a glass surface at a constant 5,000 rpm.

Using the largest dilution ratio in Figure 4.12, a thin layer of PDMS was spun onto the surface of the Ti-Ni plate and cured to an approximate thickness of 500 nm. Next, the PDMS microchannel was adhered to the thin layer through plasma treatment. A strong bond was found between the PDMS microchannel and the thin layer. However, once fluid was pumped into the channel, adhesion between the thin PDMS layer and the Ti-Ni plate failed creating leakage. Due to the very low surface R_a of the polished alloy, good adhesion could never be formed between the Ti-Ni plate and the microchannel.

Another method attempted was a stamp and stick method to glue the microchannel on the Ti-Ni plate. First, a thin layer of an adhesive agent was spun onto a glass substrate. Next the PDMS microchannel was pressed onto the thin layer of adhesive to coat the bottom of the PDMS slab and then clamped onto the Ti-Ni substrate and cured. This procedure was attempted with super glue, PDMS and an acrylic hardening liquid. Sufficient adhesion was found in the acrylic liquid that would allow for fluid flow. Due to the crude nature of the stamp and stick method, a uniform layer of adhesive was difficult to obtain which led to the formation of pockets around the channel where the fluid could seep. In addition, flooding the channel with the adhesive agent became a problem due to the small scale of the channel which blocks any fluid flow. Also the bond between the adhesive and Ti-Ni plate eventually gave out due to the low surface R_a of the plate not allowing for the adhesive to grip the metal surface. Ultimately this method was unusable due to the limitations above that gave at best an unstable fluid flow.

To overcome the adhesion problem between the Ti-Ni plate and the PDMS microchannel, a system was developed that used compressive force to clamp the channel to the metal. Figure 4-13 shows an illustration of the setup of the system; a PDMS microchannel was sandwiched between the Ti-Ni plate and an acrylic top piece. Holes were precut in the acrylic to allow for luer stubs to be inserted into the entrance and exits. To apply the compressive force to the stack of acrylic, PDMS and Ti-Ni, the components were clamped together with black binder clips. The acrylic piece served to create a more uniform compressive force on top of the PDMS slab. Once clamped, the thermal heater was adhered to the bottom of the stack using thermal paste.

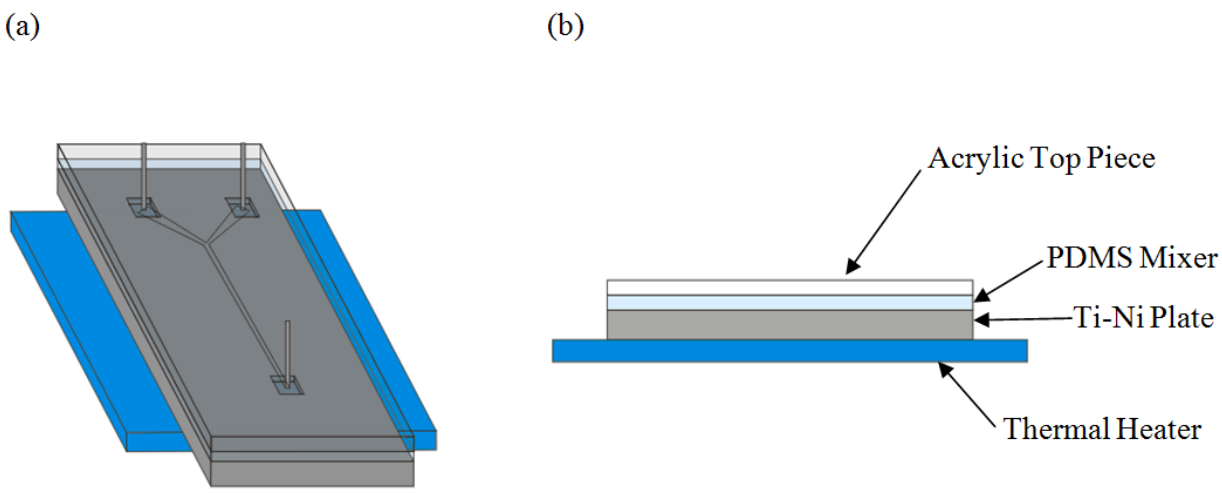

Figure 4.13: (a) Isometric drawing of the SMA micromixer assembly. (b) Cross-section showing the individual components in the assembly.

In addition to the adhesion method used, the number of features used differed from the proof of concept physical study discussed in Chapter 3. In the proof of concept study, the microfeatures were patterned along the entire length of the mixer. Due to the difficulty of creating multiple features using the indenting method discussed in this chapter, only a small array of features could be fabricated. The most significant limiting factor of the patterning process was the difficulty associated with properly lining up the individual tungsten wires to be indented.

Because the tungsten wires were only 76.2 μm in diameter, handling them was difficult. Initially an array of 10 wires was placed on the Ti-Ni surface placed at an approximate angle of 45° to the proposed direction of the channel and a spacing of 100-200μm. Then a force of 3,000 N per wire was applied to the wire array to obtain the maximum indent depth discussed in section 4.1.3. The resulting indents were very shallow and the plate showed an overall deformation around the entire area where the wires were present. Because of this effect, multiple wires could not be indented

simultaneously. To achieve an array of indentations, the wires were pressed one at time aligning a fresh wire for each feature. This led to a very time consuming process in which only ten features were indented on the Ti-Ni surface. Figure 4.14 shows three of the indents in the array before the planarization step.

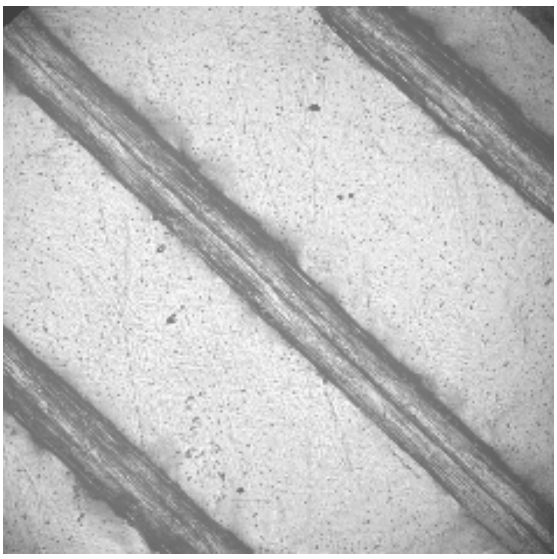

Figure 4.14: Indented array with average depth of 37µm.

The overall depth of each indent and the resulting protrusion feature height after planarization agreed with the indent depth and feature height shown in Figures 4.8 and 4.9. Once the 10 feature array was indented, the Zygo interferometer was used to characterize the features and the entire Ti-Ni system was assembled.

4.3 Experimental Setup

The experimental setup for the Ti-Ni physical model was similar to the set up of the proof of concept physical study except for the following changes. First the assembly of the mixer was different due to the use of the acrylic plate used to compress the PDMS channel to the Ti-Ni plate. The luer stubs for the entrance and exit flow were still

inserted directly into the PDMS ports through holes cut out in the acrylic top piece. The system also had a thermo-electric heater incorporated into the micromixer assembly that was used to control the microfeatures on the Ti-Ni surface. These key differences are shown in Figure 4.15 below. The resulting system allowed for sufficient compressive force to contain the fluid within the microchannel creating a continuous, steady flow.

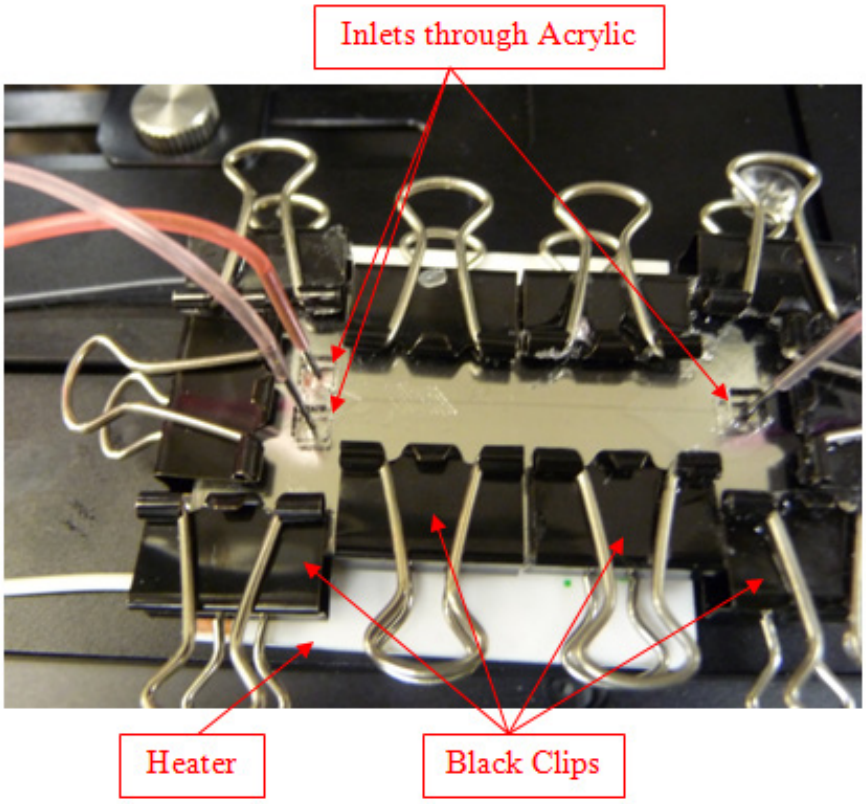

Figure 4.15: Actual physical system with acrylic, PDMS, and Ti-Ni plate clamped together with thermal heater placed below.

Another change to the experimental setup from the proof of concept physical setup was the use of a different microscope. In the proof of concept study an inverted confocal microscope was used that had the objective below the sample and the laser

signal on top of the sample. Since the Ti-Ni alloy is completely opaque, it was impossible to image this setup with the previously used equipment; instead, a fluorescent microscope was used that had its objectives and the excitation signal coming from the bottom of the sample. Since the objectives were under the imaging table, the setup had to be inverted to obtain images. Figure 4.16 shows the inverted system mounted on the microscope table.

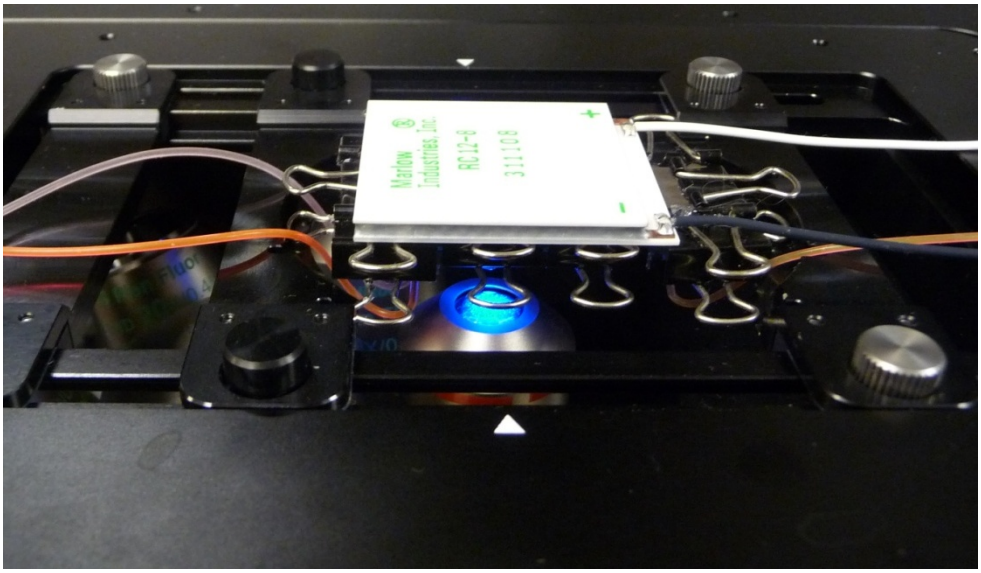

Figure 4.16: Inverted SMA micromixer assembly on microscope table. The objective lenses and fluorescent signal are both below the assembly.

Although the SMA micromixer could be imaged using this microscope, it did not have confocal capabilities. Therefore, only top down images could be taken of the fluid flow, and no cross-sectional images were obtained.

4.4 Experimental Results

Other than the differences in microscope and the micromixer assembly outlined in the previous section, the general procedure used for the SMA micromixing experiments was identical to the steps outlined for the proof-of-concept micromixer in section 3.3.

The Ti-Ni slanted groove micromixer was intended to function by using microfeatures within the channel to create a rotational flow and increase mixing efficiency. By creating these features on a SMA surface, the rotational flow could be turned on and off by changing the ambient temperature. However, problems were encountered when trying to test the system above the transition temperature.

The start of the Austenite phase transition of the bulk Ti-Ni is around 77.8°C, but the transition does not finish until 131.8°C. In practice, the transition temperatures needed for the microfeatures to fully protrude was closer to 150-160 °C, making this system incompatible with water. At a temperature below 100°C, , the features would not fully protrude and had little impact on the fluid flow. At or above 100°C, bubbles formed in the channel due to water vapor formation. In general in any liquid that would have a boiling point above the 160°C transition temperature would be too viscous to flow through the microchannel. Therefore, images were only obtained up to a temperature around 90°C when the features were beginning to protrude. Figure 4.17 shows an optical micrograph of the partially protruded features in the microflulidic channel.

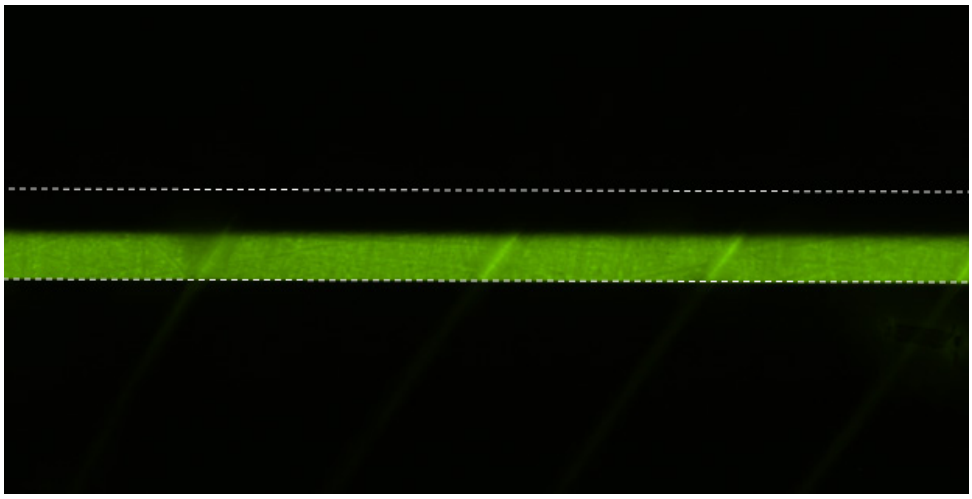

Figure 4.17: Partially protruded Ti-Ni features in a 200 µm wide microchannel.

Figure 4.17 shows that the effect of the features at 90°C on fluid flow was negligible. This is due to the minimal protrusion of the SMA features at temperatures below the boiling point of water. Using the available materials a complete micromixer using a Ti-Ni alloy was not possible due to the high transitions temperature for the SMA. However, in the future a low transition temperature SMA could potentially be used for this system.

Chapter 5: Conclusion and Future Work

5.1 Conclusion

Overall the SMA micromixer design presented in this paper represents a possible method to achieve a controllable chaotic micromixer. Although a complete system was not realized in this study, the shortcomings were due to a limited number of factors that in future work could potentially be corrected to obtain a fully functional micromixer. The main limiting factor was the high transition temperature (160° C) for the shape memory alloy used in this demonstration, so fluid could not flow through the combined heated system without turning into water vapor. But both of the key components of the system: temperature controlled SMA features and the mixing effect through the SGM design, were individually successful.

An important step in the creation of a fully functional system was proving that a rotational flow could be created with low profile microfeatures. In similar studies, patterns used to create rotational flow in similarly sized microchannels had a feature height to channel height ratio around 0.3-0.5, as compared to a ratio of 0.1 used in this study. Both computational and physical proof of concepts studies presented in this paper use a 0.1 ratio and still showed a significant rotational flow created by the slanted groove features. For the physical study the SGM features rotated the flow 180° for every 10-11 mm of distance from the inlet. In addition, the computational simulation showed increased vorticity at the feature interface as well as a rotational velocity profile after one cycle (10 features) of the rounded features that were modeled after the Ti-Ni indentation profile. Despite the inability to demonstrate a completely integrated system, the Ti-Ni

SMA surface was successfully characterized with reversible microfeatures controlled by temperature. By mechanically indenting and subsequently polishing the surface of the SMA, protruding microfeatures with a 5-7 μm approximate height were obtained. Additionally an array of 10 features was created by indenting the sample multiple times producing distinct individual features. But limitations of the fabrication process of the microfeatures on the Ti-Ni surface made it difficult to achieve repeatable feature placement and indent depth. This led to variable spacing distances between features, feature angle and height. Improvement of this process could lead to better accuracy of placement as well as more consistent indentation depths and thickness from indent to indent.

But ultimately the major limiting factor of this particular completed system was the high transition temperature of the Ti-Ni features. This particular alloy cannot show fully protruded features at temperature low enough to be compatible with water. This made it impossible to visualize the impact of the SMA features on mixing in the completed microfluidic system.

5.2 Future Work

Despite the inability to generate a tunable micromixer with this particular shape memory alloy, there are multiple areas for future work using SMA as a means of controlling a microfluidic mixing device. There are also many areas for future work into the effects of the SGM and other mixer designs in microfluidic devices. In addition, there are opportunities to further explore the characteristics of the reversible nature of Ti-

Ni shape memory alloys. Some of the most promising areas of future work are listed here:

1. ***Other shape memory alloys.*** Although this particular study used a specific Ti-Ni alloy to produce the reversible features, many other alloys demonstrate shape memory behavior and have different transition temperatures. This could allow for the complete formation of the protruded features at a lower temperature when using a different alloy. It may also be possible to obtain taller mixing features with a different alloy.
2. ***New channel design.*** In this study a channel height of 70 μm and width of 200 μm was used because it was similar in size to chaotic micromixers in previous studies. With the low profile restriction of this study, an increased effect may be seen with a channel that has a smaller cross-sectional area. This could be created by reducing both the height and width together or independently to study the effects of both dimensions. A smaller channel size may show measurable rotational flow even with very small feature profiles.
3. ***New mixing feature design.*** In this study the geometry of the SGM used was chosen because of the limitations of the SMA features. When looking at the SGM design parameters such as feature angle, feature width, feature spacing, feature height, channel height, channel width, mixer length and fluid velocity can all be varied. Without the limitations of having to adhere to once particular height or width, the effects of all these parameters could be studied. This could show the significance that each parameter has on the flow and lead to an overall guide to optimizing the SGM given certain parameters.

4. ***Improved microfeature fabrication methods.*** The fabrication process for the microfeatures on the SMA surface for this study was based off of previously proven methods. Although this method can produce significant microfeature protrusions, it is increasingly difficult to accurately pattern then features close together. In addition the wire used tended to deform, giving variations in indent depth and width leading to variations in protrusion height. The use of a wire that can take a larger compressive load could lead to increased repeatability of each feature. Other possible indentation methods could also explored to create better pattern fidelity when trying to create an array of features. This could come in the form of a patterned punch. Another possible solution could come in the form of using a softer SMA material, making it easier to indent.
5. ***Alternative PDMS / SMA adhesion methods***. Adhesion methods used in traditional microfluidic devices composed of PDMS channels and glass or silicone substrates show superior adhesion. But when trying to bond a PDMS channel to a polished metal surface most attempts using adhesives were unsuccessful. The resulting system using compression to seal the microchannel was bulky compared to the size of the systems consisting of only glass and PDMS. The systems were also often had an unreliable seal. If a reliable method for adhering the microchannels to a metallic surface was created, it would simplify the overall process for creating a SMA micromixer.

APPENDIX A

Procedures: Two-Step Photolithography Fabrication Process

Note: All steps outlined are performed in a clean room environment to reduce risk of environmental and user contamination of the microfabrication process.

Note: SU-8 developer should be handled inside a fume hood and disposed of properly.

Note: All specifications for spinning speed, bake temperatures and exposure times are outlined in manufacturing specifications from MicroChem corporation.

1. Surface Preparation

a. Prepare Silicone wafer by cleaning surface of foreign particles with nitrogen jet.
b. **Note:** Always use wafer tongs when handling Si-wafers to minimize contamination of the wafer.

2. Coating

a. Mount Si-wafer on spin-coater chuck ensuring that there is a proper vacuum seal. Center the wafer on the chuck by running test spins until adequately centered.
b. Pre-set spinning cycle to proper ramp time and spinning speeds before dispensing SU-8. Spinning speeds and resulting feature heights are detailed on SU-8 specification sheets.
c. Dispense 1cc of SU-8 per inch of radius of the wafer onto the center of the wafer. Take care to ensure no foreign particles or bubbles are present in dispensed SU-8.
d. Close the cover of the spin-coater and run the pre-set program, once the program is finished an even, uniform coat of SU-8 should be present.

3. Soft-Bake

a. Remove Si-wafer from spin-coater and place wafer on pre-heated hotplate for required time for soft-bake.
b. Once soft-bake is complete place the wafer on a room temperature surface and allow wafer to fully cool. Once cooled the SU-8 layer should be completely hardened.

4. Alignment

a. Place pre-fabricated photomask in mask-aligner machine. Ensure that the side in which the mask is printed on will be in contact with the wafer. This will allow for the tightest tolerances possible on features to be created.
b. Place the Si-wafer into the mask aligner with hardened SU-8 surface facing towards the photomask and light source.

c. Align the features on the photomask to the center of the wafer.
d. Bring the Si-wafer into contact with the photomask.

5. Exposure

a. Expose the photomask and Si-wafer to UV-light for appropriate exposure time.

6. Post-Bake

a. After exposure, carefully remove the wafer from the mask aligner and place wafer on pre-heated hotplate for required post-bake time.
b. Note: A few minutes into the post-bake the outline of the micro patterns should start to appear in the SU-8.
c. Once soft-bake is complete, place the wafer on a room temperature surface and allow wafer to fully cool. Once cooled the SU-8 layer should be completely hardened and the first layer of the two layer process is complete.

7. Coating Layer 2

a. For the second layer, repeat procedures detailed in Step 2 with the correct SU-8 needed for desired height profiles of layer 2.
b. Note: Due to the slick surface of the first layer of SU-8 any ramp time should be removed from spin coater settings, instead the program should be set to immediately accelerate to final spin speed.

8. Soft-Bake Layer 2

a. For second layer repeat procedures detailed in Step 3.

9. Alignment Layer 2

a. Repeat procedures a and b from Step 4.
b. Using the microscope on the mask aligner, bring the features on the second layer of the photomask into focus.
c. Slowly bring Si-wafer closed to the photomask until the outlines of the first SU-8 layer also come into focus.
d. Using the feature geometry and alignment marks position the Si-wafer using x,y and rotational controls bring the Si-wafer and photomask into proper alignment.
e. Bring the Si-wafer into contact with the mask, re-check the alignment to ensure that the wafer did not move in the x,y plane while making contact.
f. Note: Alignment of the second-layer is often the most difficult and time consuming task.

10. Exposure Layer 2

a. Repeat procedures detailed in Step 5.

11. Post-Bake Layer 2

12. Repeat procedures detailed in Step 6.

13. SU-8 Stripping

a. After the Si-wafer is cooled from post-bake procedures submerge the wafer in a beaker SU-8 Developer to remove all SU-8 that was not permanently cross-linked.
b. Develop for appropriate time as outlined on SU-8 specification sheets.
c. Note: Agitation of the wafer in the developer solution will greatly reduce development time.
d. At the end of development time rinse Si-wafer and SU-8 micro structures with IPA, if a white residue appears on the micro structures further development time is needed, place the wafer back in the developer. Once no white residue is present at IPA, rinse development process is done.
e. Sub-merge Si-wafer in a beaker of clean SU-8 developer solution to further rinse and clean the micro structures.

14. Cleaning

a. Use a nitrogen gun to clean of excess developer on the Si-wafer.

APPENDIX B

Procedures: PDMS Micromixer Fabrication

1. Molding Channels

a. Mix desired amount of PDMS in a 10:1 ratio of silicone gel and curing agent respectively. Mixing amount depends on mold size and desired thickness.

b. Mix thoroughly for 1-2 minutes; it should appear very cloudy and filled with air bubbles.

c. Place mixed PDMS in vacuum chamber for 30-60 minutes to remove all air bubbles.

d. Secure acrylic gasket to top of Si-wafer using black binder clips. Ensure that the seal is tight to minimize any leakage.

e. Clean wafer surface with nitrogen gun to remove all foreign particles to minimize contamination.

f. Pour degassed PDMS into mold holding the edge of the container close to the surface of the wafer to reduce additional bubble formation. If bubbles are formed, de-gas the pored mold until all bubbles are removed.

g. Place mold into oven at 100°C for 10 minutes or until PDMS is cured.

h. Remove PDMS and mold from oven and allow to cool to room temperature.

2. Mixer and Substrate Preparation

a. After PDMS and wafer have cooled, gently peel the PDMS from the wafer. Take care to not break the wafer. (Note: at higher temperatures the silicon is more brittle.)

b. Place PDMS mold on cutting surface and use razor blade to cut out mixers leaving ample space around the features for adhesion.

c. Punch entrance and exit holes in the mixer using luer stubs.

d. Prepare mounting slides and mixers for adhesion by rinsing with DI water then IPA then dry with nitrogen gun. Also clean an additional glass slide, which will be needed to place the mixers and smaller mounting slides on.

3. Plasma Bonding

a. Place mixers and slides into the plasma chamber with sides to be bonded together facing up.

b. Turn the vacuum pump and power source to the plasma chamber on by flipping the toggle switch to on.

c. Place the vacuum chamber cover on the open face sealing the chamber. Make sure the needle valve attached to the cover is completely closed.

d. Allow 1-2 minutes for vacuum to form. Slightly open the needle valve allowing air to bleed into the vacuum.

e. Turn the plasma toggle switch on and turn the knob to high.

f. Expose to air or oxygen plasma for 60-90 seconds.

g. Remove pieces from plasma chamber and place the bonding side of the PDMS face down on the mounting slide.

h. Gently press mixer down to remove visible air pockets. Take care not to apply too much pressure which can result in the channel collapsing.

i. Wait 10-15 minutes before using the channel in any experiments.

REFERENCES

[1] Nguyen, Nam-Trung, et al., *Micromixers-a review.* Micromechanics and Microengineering, 2005. 15, p. R1-R16.

[2] Stone, H.A., et al., *Engineering Flows in Small Devices: Microfluidics Toward a Lab-on-a-chip.* Annual Review Fluid Mechanics, 2004. 36, p. 381-411.

[3] Wilcox, David, *Basic Fluid Mechanics.* DCW Industries, Incorporated, 2010

[4] Patankar, Suhas V. (1980). *Numerical Heat Transfer and Fluid Flow*. New York: McGraw-Hill. p. 102.

[5] Stroock, Abraham D., et al., *Chaotic Mixer for Microchannels.* Science, 2002. 295, p. 647-651.

[6] Hessel, Volker, et al., *Micromixers-a review on passive and active mixing principles.* Chemical Engineering Science, 2005. 60, p. 2479-2501.

[7] Veenstra, TT, et al., *Characterization Method for a New Diffusion Mixer Applicable in Micro Flow Injection Analysis Systems.* Micromechanical and Microengineering, 1999. 9, p. 199-202.

[8] Bessoth, Fiona G., et al., *Microstructure for Efficient Continuous Flow Mixing.* Anal. Commun., 1999. 26, p. 213-215.

[9] Miyake, Ryo, et al., *A Highly Sensitive and Small Flow-Type Chemical Analysis System with Integrated Absorptiometric Micro-Flowcell.* IEEE, 1997. p. 102-107.

[10] Stone, Z.B., et al., *Imaging and Quantifying Mixing in a Model Droplet Micromixer.* Physics of Fluids, 2005. 17, 063103.

[11] Deshmukh, Ajay A., et al., *Continuous Micromixer with Pulsatile Micropumps.* Technical Digest of the IEEE Solid State Sensor and Actuator Workshop, 200. p. 73-79.

[12] Glasgow, I., et al., *Enhancement of Microfluidic Mixing Using Time Pulsing.* Lab on a Chip, 2003. 3, p. 114-134.

[13] Yang, Zhen, et al., *Ultrasonic Micromixer for Microfluidic Systems.* Sensors and Actuators A, 2001. 93, p. 266-272.

[14] Liu, Robin H., et al., *Bubble-Induced Acoustic Micromixing.* Lab on a Chip, 2002. 2, p. 151-157.

[15] Niu, Xize, et al., *Efficient Spatial-temporal Chaotic Mixing in Microchannels.* Micromechanics and Microengineering, 2003. 13, p. 454-462.

[16] Bau, Haim H., et al., *A Minute Magneto Hydro Dynamic (MHD) Mixer.* Sensors and Actuators B, 2001. 79, p. 207-215.

[17] Mao, Hanbin, et al., *A Microfluidic Device with a Linear Temperature Gradient for Parallel and Combinatorial Measurements.* Journal of American Chemistry Society, 2002. 124, p. 4432-4435.

[18] Ni, W.Y., Cheng, Y.T., et al., *Microscopic Super Elastic Behavior of a Nickel-Titanium Alloy Under Complex Loading Conditions.* Applied Physics Letters, 2003. 82, 2811.

[19] Zhang, Yijun, et al., *Shape Memory Surfaces.* Applied Physics Letters, 2006. 89, 041912.

[20] Otsuka, K, et al., *Shape Memory Materials.* Cambridge University Press, 1998.

[21] Oshida, Y, et al., *Corrosion and Biocompatibility of Shape Memory Alloys.* Zairyo-to-Kankyo (Corrosion Engineering), Dec. 1991, Vol. 40, no.12, p. 834-844.

[22] Lagoudas, Dimitris, *Shape Memory Alloys: Modeling and Engineering Applications.* Springfield, 2008.

[23] Mabe, J., *Variable area jet nozzle for noise reduction using shape memory alloy actuators.* Acoustics 2008, Paris.

[24] Madou, Marc, *Fundamentals of Microfabrication: the Science of Minturization 2nd Edition.* CRC Press, Boca Rotan, Fl., 2000.

[25] Microchem, Kayaku Microchem, *SU-8 3000 Data Sheet: Permanent Epoxy Negative Photoresist.*

[26] Jo, Byung-Ho, et al., *Three Dimensional Micro-Channel Fabrication in Polydimethylsiloxane (PDMS) Elastomer.* Journal of Microelectromechanical Systems, March 2000, Vol. 9, No. 1.

[27] Yang, Fuqian, Cheng, Yang-Tse, *Revisit of the Two-Dimensional Indentation Defprmation of an Elastic Half-Space.* J. Mater. Res., June 2009, Vol. 24, No. 6.

[28] ISO 6344-1, *Coated Abrasives, Sizes and Tests.* 1998.

[29] e-Funda, *S7 tool steel.http://www.efunda.com/materials/alloys/tool_steels/show_*

tool.cfm?ID=AISI_S7&prop=all&Page_Title=AISI%20S7. 2011.

[30] Lassner, Erik, et al., *Tungsten: Properties, chemistry, technology of the element, alloys, and chemical compounds*.

[31] Thangawng, Lebi, *An ultra thin PDMS membrane as a bio/micro-nano interface: fabrication and characterization.* Biomed Microdevices, 2007, Vol. 9, 587-595.

[32] Ashim, Data, *An Introduction to Modeling of Transport Functions.* Cornell University, New York.

[33] Kim, Dong, et al., *A barrier embedded chaotic micromixer.* Journal of Micromechanics and Microengineering, 2004, Vol. 14, p. 798-805.

[34] Gobby, D, et al., *Mixing characteristics of T-type microfluidic mixers.* Journal of Micromechanics and Microengineering, 2001, Vol 11, p. 126-132.

[35] Li, Zhang, et al., *On the mutual diffusion properties of ethanol-water mixtures.* The Journal of Chemical Physics, 2006, Vol. 125.

[36] Kamholz, Andrew, et al., *Quantitative Analysis of Molecular Interaction in a Microfluidic Channel: The T-Sensor.* Journal of Anal. Chem., 1999, 71, 5340-5347.

Education

Bachelors of Science, College of Engineering, Department of Mechanical Engineering, University of Kentucky, Lexington, KY, May, 2009.

Positions Held

Design Engineer, Jacobs Vehicle Systems, Bloomfield, CT, 2011.

Research Fellowship, University of Kentucky, College of Engineering, Precision Biosystems Lab, Lexington, KY, 2009-2011.

Design Engineer, Belcan Aerospace, Lexington, KY, 2007-2008.

Presentations

Lilly, D. (2009) *Design and Optimization of Low-Profile Passive Microfluidic Mixing Geometry.* Presented in a Micro-Electro Mechanical poster session at ASME Conference, Orlando, FL.

Honors and Awards

University of Kentucky, full scholarship, 2009-2011.